frontiers | Frontiers in Marine Science

Geochemistry of Hydrothermal Fluids From the E2-Segment of the East Scotia Ridge: Magmatic Input, Reaction Zone Processes, Fluid Mixing Regimes and Bioenergetic Landscapes

Samuel I. Pereira[1,2,3]*, Alexander Diehl[1,2], Jill M. McDermott[4], Thomas Pape[1,2], Lukas Klose[5], Harald Strauss[6], Gerhard Bohrmann[1,2] and Wolfgang Bach[1,2]

[1] Faculty of Geosciences, University of Bremen, Bremen, Germany, [2] MARUM-Center for Marine Environmental Sciences, Bremen, Germany, [3] Department of Earth Sciences & Centre for Deep Sea Research, University of Bergen, Bergen, Norway, [4] Department of Earth and Environmental Sciences, Lehigh University, Bethlehem, PA, United States, [5] Department of Physics and Earth Sciences, Jacobs University, Bremen, Germany, [6] Department of Geology and Palaeontology, University of Münster, Münster, Germany

The compositions of hydrothermal fluids in back-arc basins (BABs) can be affected by the influx of magmatic fluids into systems that are dominated by reactions between basement rocks and seawater-derived fluids. The East Scotia Ridge (ESR) in the Scotia Sea hosts such hydrothermal systems where the role of magmatic fluid influx has not yet been addressed. During expedition PS119 in 2019, three chimneys were sampled from the E2 segment. These samples were analysed for their chemical and isotopic composition along with fluid inclusions in corresponding precipitates. Our data provide evidence for the temporal evolution of hydrothermal fluids in this remote back-arc system. Salinity variations in anhydrite-hosted fluid inclusions indicate that phase separation takes place in the subseafloor. Moderate-temperature (<53°C) fluids from the newly discovered E2-West hydrothermal vent field and high-temperature (>320°C) fluids from the E2-South area were sampled. Depletions in fluid-mobile elements, ΣREE and low $\delta^{18}O_{H2O}$ show that the basement in this root zone has been leached since the previous sampling in 2010. The results indicate that high-temperature fluid-rock interactions are key in setting the composition of the fluids with cation-to-chloride ratios suggesting a common root zone for both vent sites. The concentrations of dissolved gases provide new insights in the connection between magmatic degassing and its influence on endmember vent fluid composition. Specifically, stable isotope (O, H) data and elevated CO_2 concentrations point to a minor influx of magmatic vapour. Stable sulphur isotopes provide no evidence for SO_2 disproportionation suggesting a H_2O-CO_2 dominated nature of these vapours. The concentrations of conservative elements in the E2-W fluid reflects subseafloor mixing between E2-S endmember fluid and seawater. In contrast, non-conservative behaviour,

and depletion of Fe, H_2, and H_2S point to a combination of sub-surface abiotic and biotic reactions affecting these fluids. Similarly, E2-W fluids show evidence for H_2S and CH_4 being metabolized in the subseafloor. Thermodynamic computations confirm that the E2 system is dominated by sulphide oxidation as a major catabolic pathway. Our results indicate that the conditions at E2 are favourable to hosting a robust subseafloor biosphere.

INTRODUCTION

Back-arc basin (BAB) hydrothermal systems emit fluids with compositions that can be distinct from their mid-oceanic ridge (MOR) counterparts. Besides being affected by fluid-rock interactions and phase separation, they are often influenced by the addition of gases and volatile elements from magmatic fluid influx (e.g., De Ronde and Jambor, 1995; Ishibashi and Urabe, 1995; Yang and Scott, 2006; Reeves et al., 2011; Seewald et al., 2015; Seewald et al., 2019). Magma degassing typically adds H_2O and CO_2 to the circulating seawater-derived fluids (e.g., Lupton et al., 2006; Reeves et al., 2011), but may also deliver acid-sulphate components such as SO_2, HCl and HF (Butterfield et al., 2011; Seewald et al., 2015; Seewald et al., 2019). This addition of magmatic components can influence fluid-rock interactions and also have an effect on dissolved metal concentrations (Reeves et al., 2011; Seewald et al., 2015; Seewald et al., 2019).

The majority of BAB hydrothermal systems are situated in the western Pacific, e.g., Manus Basin, Okinawa Trough, Lau Basin (Takai et al., 2008; Mottl et al., 2011; Reeves et al., 2011; Seewald et al., 2015; Seewald et al., 2019). The East Scotia Ridge (ESR) in the Southern Ocean is the only known BAB to host active hydrothermal systems outside the Pacific (Diehl and Bach, 2020b; Diehl and Bach, 2021). Located in an area where the Atlantic, Pacific and Indian oceans merge, hydrothermal vent sites of the ESR may be important biogeographic stepping stones for vent fauna (Rogers et al., 2012; Herrera et al., 2015). Like in other hydrothermal areas in the deep sea, the foundation of life around the ESR vents are chemosynthetic microorganisms that metabolize reduced gases and metals dissolved in the vent fluids (Rogers et al., 2012; Linse et al., 2019). Establishing the most important catabolic energy sources brought into these ecosystems by hydrothermal venting is hence vital. Existing vent fluid data for the E2-segment of the ESR system (James et al., 2014) shows that the composition of the fluids venting in 2010 were affected by fluid-rock interactions, phase separation and conductive cooling prior to venting at the seafloor, but the contents of dissolved gases (CO_2, H_2 and CH_4) were not determined in previous studies (Cole et al., 2014; James et al., 2014).

During the *RV Polarstern* expedition PS119 (Bohrmann, 2019) a total of three chimneys were sampled from the known E2-South (E2-S) vent site (James et al., 2014) and a newly discovered vent site (E2-West) to the northwest. The use of gas-tight fluid samplers facilitated measuring the contents of

dissolved gases, which is critical for constraining magmatic degassing (e.g., Reeves et al., 2011), and *in situ* pH, vital for examining fluid-rock reactions (e.g., McDermott et al., 2018). Dissolved gases are also a key source of energy for catabolic reactions that control chemolithoautotrophic biomass production in these ecosystems (e.g., McCollom and Shock, 1997; Amend et al., 2011; Dahle et al., 2015; Dahle et al., 2018).

The goal of this study is to provide constraints on gas concentrations, as they hold clues about magma-hydrothermal interactions and are important for the bioenergetic landscape of the vent system. Also, the first re-sampling of the vents at E2-S since 2010 (Cole et al., 2014; James et al., 2014), allowed us to determine if vent fluid composition had changed between then and 2019.

GEOLOGICAL SETTING

The East Scotia Ridge (ESR) is a back-arc spreading centre hosted in the Scotia Sea at the northernmost edge of the Southern Ocean (**Figure 1**). The spreading activity is a result of the subduction of the South American plate under the Sandwich plate (German et al., 2000). The ESR is spreading at a rate of 62-70 mm/yr and separates the Scotia plate from the Sandwich plate (Livermore et al., 1997; Larter et al., 2003). The spreading centre can be broadly divided into sub segments E1 to E9 from north to south, respectively (Livermore et al., 1997). The central part of the ESR has a distinct axial valley graben, and features rocks with a composition similar to mid-oceanic ridge basalts (MORBs, Fretzdorff et al., 2002; Leat et al., 2004). The northern and southern parts of the ESR have axial volcanic ridges (AVRs), that likely reflect a higher magma budget and may relate to mantle inflow into the back-arc due to a roll-back induced corner flow of mantle material around the subducting slab (Livermore et al., 1997; Leat et al., 2000; Bruguier and Livermore, 2001). Seismic reflectors at the E2 segment show evidence for the presence of an axial magma chamber at ca. 3 km below seafloor (Livermore et al., 1997) and corroborate enhanced magma supply rates and high crustal heat flux. Indeed, hydrothermal activity was found at the E2 segment with hydrothermal vent sites hosted on one such axial volcanic ridge (German et al., 2000; James et al., 2014). The basement is primarily composed of basaltic andesite with increased Pb concentrations compared to MORBs, suggesting an influx of
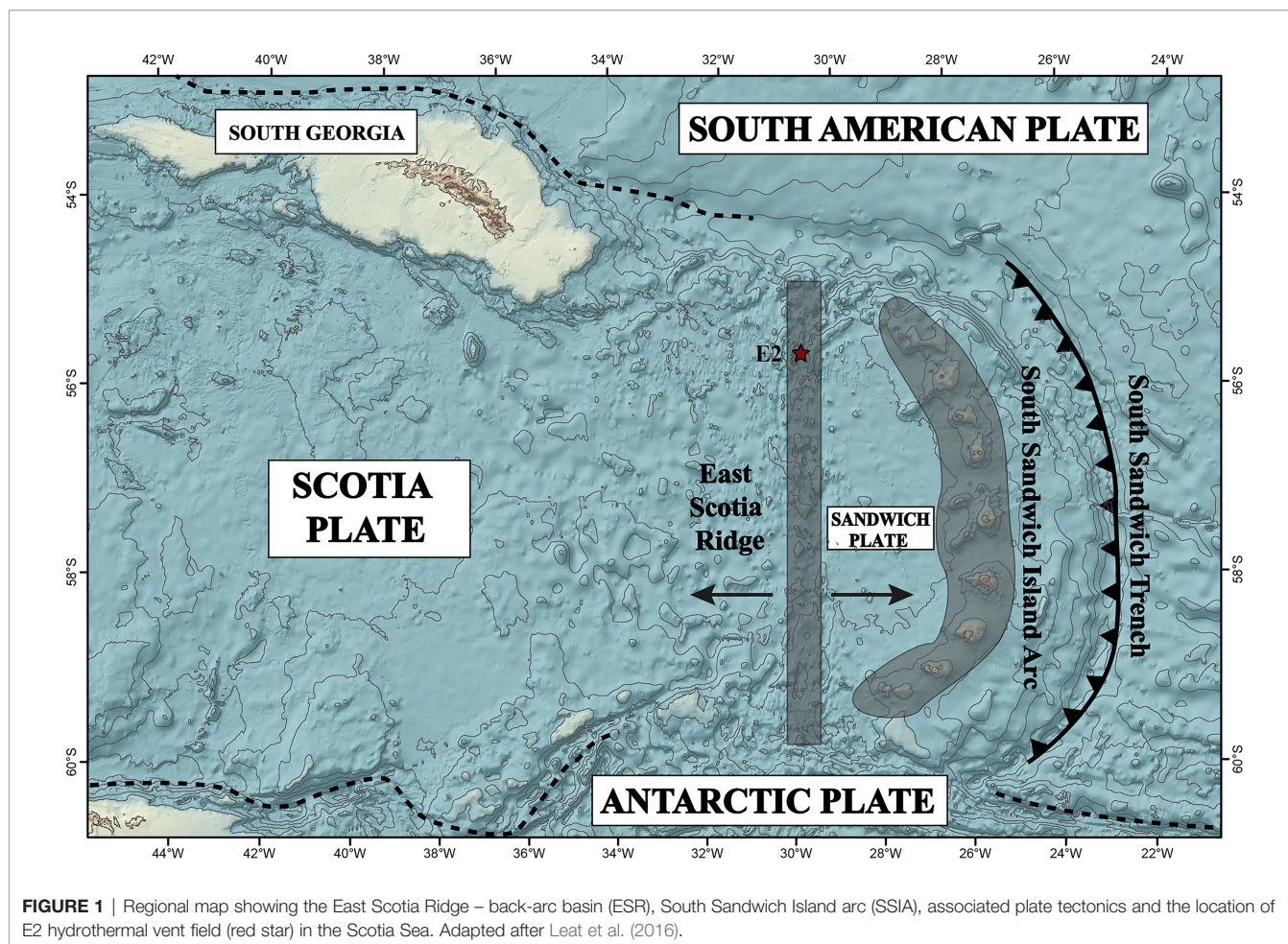
FIGURE 1 | Regional map showing the East Scotia Ridge – back-arc basin (ESR), South Sandwich Island arc (SSIA), associated plate tectonics and the location of E2 hydrothermal vent field (red star) in the Scotia Sea. Adapted after Leat et al. (2016).

slab-derived components (Leat et al., 2000; Fretzdorff et al., 2002; Leat et al., 2004).

The E2-S hydrothermal vent field was discovered in 2009 (Rogers et al., 2012) and low (<20°C) and high (>310°C) temperature fluids were first sampled in 2010 (James et al., 2014). It is situated between 56°05.2' to 56°05.4'S and 30°19.0' to 30°19.35'W in 2600 m water depth between two N-S-striking AVRs exposing pillow lavas of basaltic andesite composition. Two vent sites were sampled in 2010: (1) Dog's Head, a small cluster of ~12-m tall chimneys venting black-smoker type fluids with temperatures as high as 351°C, and (2) Sepia, which is 75 m southwest of Dog's Head, and had fluids (up to 353°C) venting from a 11-m tall bulbous chimney with several flanges, underneath which hot (311°C) fluids pooled (James et al., 2014).
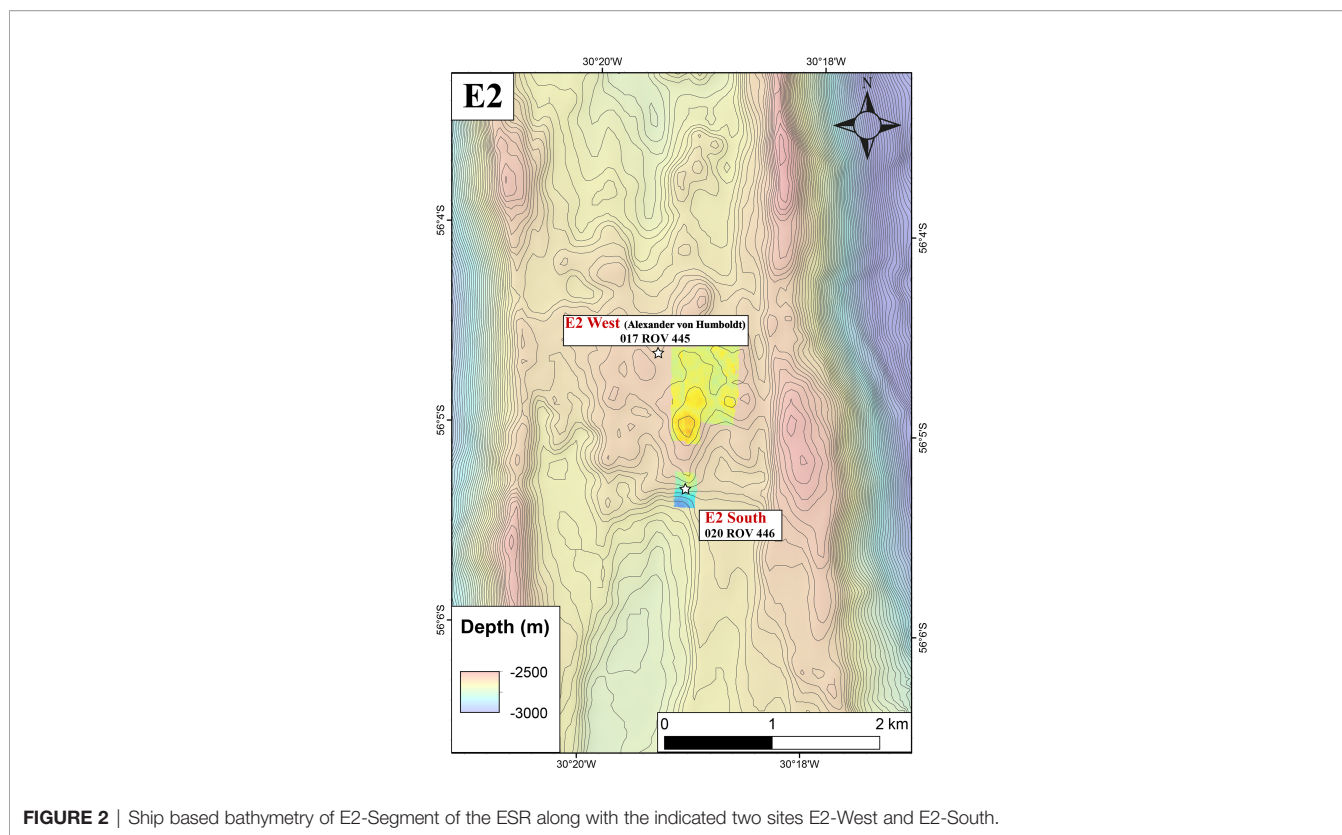
MATERIALS AND METHODS

High and low-temperature hydrothermal fluid samples were collected during expedition PS119 with *RV Polarstern* in April-May 2019. We found hydrothermal activity to the northwest of the sites visited by James et al. (2014). We hence distinguish between E2-S vent area (which includes the Dog's Head and Iced

Bun sites) and E2-W ('Alexander von Humboldt' hydrothermal vent field) which is a newly discovered site (**Figure 2**).

The Iced Bun site had not been sampled previously and was actively venting black smoker-type fluid (T_{max} = 320°C, **Figure 3A**). It is in the southern part of the E2-S vent area (56°05.30'S and 30°19.12'W) at a water depth of 2700 m, 20 m west of the Sepia sites and ca. 60 m southeast of the Dog's Head site, both of which were sampled by James et al. (2014). Dog's Head in the northern part of the E2-S vent area (56°05.28'S and 30°19.14'W) is a small cluster of chimneys with several orifices emitting black smoker-type fluid (**Figure 3B**). We recorded a maximum temperature (T_{max}) of 344°C which was lower than the T_{max} of 351°C measured in 2010 (James et al., 2014).

E2-W is situated between 56°04.57' to 56°04.63'S and 30° 19.42' to 30°19.33'W (ca. 1.2 km north-northwest of the E2-S system) at a water depth of 2500 m and covers an area of ca. 1600 m^2 (**Figure 2**). The entire area was venting diffuse fluids evident from shimmering water and distributions of Hoff crabs (Bohrmann, 2019). No venting of high temperature fluids was observed during the dives. In the sampled area, 30 – 50°C warm fluids were diffusely venting out of a prominent broken pillow tube structures (**Figure 3C**, Bohrmann, 2019). This structure was yellowish in colour and at places extensively covered by

FIGURE 2 | Ship based bathymetry of E2-Segment of the ESR along with the indicated two sites E2-West and E2-South.

microbial mats (**Figure 3D**). A fluid sample at E2-W was collected after a flocculent mat and the pale-yellow precipitates surrounding the orifice were removed by the submersible arm.

Sample Collection and Preparation

Fluids were recovered using 150ml titanium isobaric gas tight (IGT) samplers (Seewald et al., 2002) operated with the Remotely Operated Vehicle (ROV) *MARUM-Quest4000m*. Two fluid samples were collected at the orifices of Dog's Head and Iced Bun at the E2-S segment and one sample was recovered at the newly discovered site called 'E2-West' (Bohrmann, 2019, **Table 1**). The fluids were sampled after breaking off the tip of the chimney structure to allow for better flow of fluid. The temperature of the fluids collected with IGTs were monitored in real-time using a thermocouple attached to the IGT or with the ROV's temperature sensor immediately after fluid sampling. After recovery of the ROV, the IGTs were processed onboard to obtain the fluid as soon as possible (within 12 hours of sampling). The samples were extracted from the IGTs using a HPLC pump and analysed for concentrations of dissolved gases (H_2, CH_4 and H_2S) and $pH_{(25°C)}$.

Filtered (0.45 µm) fluid aliquots for major and trace elemental analysis were collected in acid-cleansed high density-polyethylene (HDPE) Nalgene™ bottles and acidified using 200 µL of concentrated sub-boiled HNO_3. Filtered and unacidified aliquots were collected for anion analysis and for stable hydrogen (δD_{H2O}) and oxygen ($\delta^{18}O_{H2O}$) water isotope analysis in sealed glass ampoules. To determine the total

dissolved inorganic carbon (ΣCO_2, abbreviated as CO_2 hereafter), fluid aliquots were injected from gas-tight syringes into pre-weighed He-filled and subsequently evacuated glass serum vials to prevent atmospheric CO_2 contamination. The serum vials were stored upside down to seal the septa and prevent diffuse gas loss. For determination of $\delta^{13}C$ and δD in CH_4 and $\delta^{13}C_{CO2}$, 12-15 ml of gas at standard pressure (STP) were injected into 20 ml glass serum vials containing concentrated NaCl solution. Atmospheric contact of the sample gas was prevented.

Analytical Methods: Fluid Chemistry

Concentrations of H_2 and CH_4 were determined onboard using a 7820A Agilent gas chromatograph (GC). A syringe headspace extraction was done first and the H_2 and CH_4 in the headspace gas was measured using different detectors (Reeves et al., 2011). H_2 was quantified using a thermal conductivity detector (TCD), while CH_4 was determined using a flame ionization detector (FID). The GC was equipped with a Molsieve 60/80 column (Sigma-Aldrich, St Louis, MO) and was operated with N_2 as a carrier gas at 90°C. The analytical uncertainties (2s) are considered as ±5% for H_2 and CH_4. pH (at 25°C and 1 atm) was measured potentiometrically using a 'seven2go' pH electrode (Mettler Toledo, USA) instantly after the fluid was removed from the gas-tight syringe to minimize the effect of degassing. The electrode was calibrated daily using a 4-point calibration with reference solutions of pH 2, 4, 7 and 11. The uncertainty for pH values can be considered within ±0.1 unit.
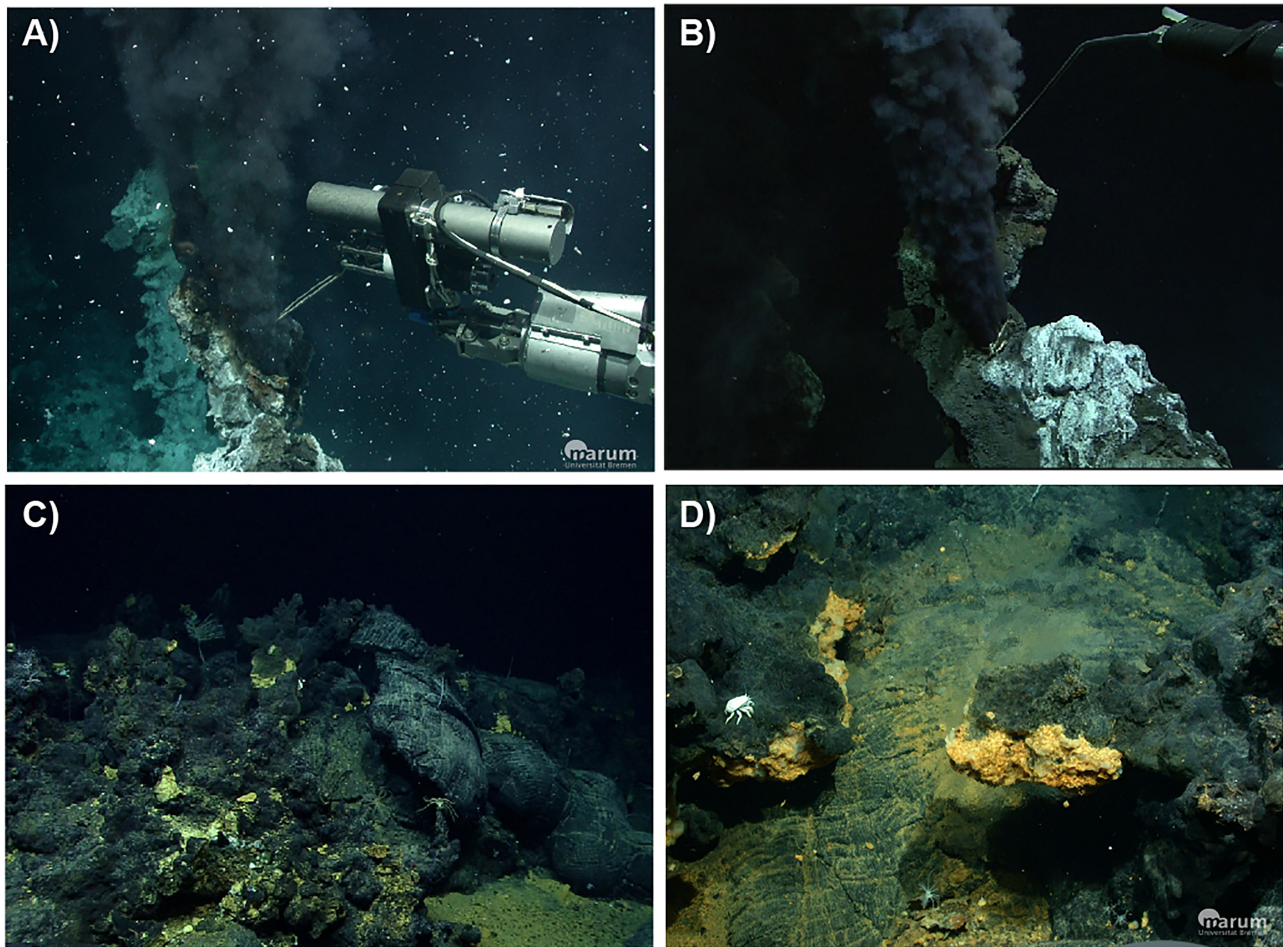
FIGURE 3 | Images of hydrothermal orifices at E2: **(A)** Iced Bun chimney; **(B)** Dog's Head Chimney; **(C)** Diffuse flows escaping from pillow basalts at E2-W **(D)** E2-W tube structure.

Concentrations of major and minor elements were determined using inductively coupled plasma optical emission spectroscopy (ICP-OES, Varian Vista Pro, radial plasma observation) and ion chromatography (IC, Metrohm CompactIC) with a 'METROSEP A Supp 5-150/4.0' column at MARUM, University of Bremen. Trace elements including rare earth elements (REEs), were determined using inductively coupled plasma mass spectroscopy (ICP-MS, Perkin Elmer NexION) at Jacobs University, Bremen. The REEs were determined following a matrix separation and a pre-enrichment method (Schmidt et al., 2010). An ion-exchange column (Sep-Pak C18 cartridge^{TM}) was used for the matrix separation. The accuracy of major and minor elements was monitored using IAPSO standard seawater (supplied by Ocean Scientific International Ltd., UK). The quality of the trace element concentration measurements was monitored using the certified reference material NASS-7 (seawater) from the National Research Council of Canada. The analytical uncertainties (2s) are ±2% for dissolved Na, Si, Mg, Cl, Br and SO_4, ±5% for dissolved Ca, F, Li, Sr, Ba, Al, Fe, Mn and K, ±8% for dissolved B, Rb, Cs and <±10% for REEs.

Total dissolved sulphide (ΣH_2S, hereafter abbreviated as H_2S) was determined gravimetrically at the Faculty of Geosciences, University of Bremen, following shipboard precipitation as Ag_2S in a 5 wt.% $AgNO_3$ solution (prepared on a daily basis) in a method adapted from Seewald et al. (2015). The estimated working range for the gravimetric method is >1mM. Low H_2S concentrations (0.2µM to 1mM) were determined photometrically using the methylene blue method by Cline (1969). CO_2 concentrations were determined onshore after the fluid samples were acidified with 25 wt.% phosphoric acid into the aliquots directing the headspace gas directly into the GC (Thermo Scientific Trace GC Ultra), which was equipped with a Haysep 80/100 column (Sigma-Aldrich, St Louis, MO) and was operated with He as a carrier gas at 50°C. This method was adapted after Reeves et al. (2011). The analytical uncertainties (2s) are considered as ±10% for CO_2 and ±15% for H_2S relative to measured values.

Stable oxygen and hydrogen isotope compositions of vent fluid H_2O were analysed using cavity ring-down spectrometry (CRDS, Picarro L-2130i) at MARUM. The measurement

TABLE 1 | Measured concentrations and isotopic composition of aqueous species from the fluids recovered at E2-South and E2-West hydrothermal vent fields. Lowest Mg fluids sampled in 2010 were added for comparison.

Edifice	Sample	T_{max} [°C] (in situ)	pH_{MIN} (25°C)	pH (in situ)	Mg mM	Na_{Meas} mM	Na_{CB} mM	K mM	Li µM	Rb µM	Cs nM	Ca mM	Sr µM	Ba µM	B µM	Cl mM	Br µM
LOQ		–	–	–	–	–	–	–	7.2	0.003	1.94	–	–	0.04	9.25	–	–
BSW	CTD10-01	0.5	7.7	7.9	51.6	460	463	10.0	25.1	1.26	2.0	9.56	82.6	0.29	399	540	820
E2-West																	
Flange	445-17ROV 03F	53	6.7	6.6	42.6	446	468	13.4	78.4	6.8	63.5	13.2	85.0	1.26	410	543	823
E2- South																	
Iced Bun	446-20ROV 07F	320	3.3	4.8	4.45	412	410	33.0	500	51.0	492	29.9	94.4	37.5	574	515	810
Dog's Head	446-20ROV 10F	344	3.2	5.3	10.5	402	407	28.9	383	42.1	373	23.3	80.5	13.7	480	501	767
E2-South[a]																	
Dog's Head[a]	JC42-132-Y1-07	351	3.1	nd	1.05	434	nd	39.8	614	nd	609	30.8	106	23.6	548	528	837
Sepia[a]	JC42-135-Y2-04	353	3.1	nd	2.04	430	nd	38.1	603	nd	590	31.8	105	15.2	537	528	848
Sepia Flange[a]	JC42-132-B1-02	313	2.9	nd	4.15	420	nd	35.8	557	nd	561	28.9	95.9	19.9	555	521	837

Edifice	Sample	F µM	Si mM	SO_4 mM	Fe µM	Mn µM	Al µM	H_2 µM	H_2S mM	$\delta^{34}S_{H2S}$ ‰	CH_4 µM	$\delta^{13}C_{CH4}$ ‰	$\delta^{2}H_{CH4}$ ‰	CO_2 mm	$\delta^{13}C_{CO2}$ ‰	$\delta^{18}O$ ‰	δD ‰
LOQ		–	–	–	0.9	–	1.85	–	0.0002	–	–	–	–	–	–	–	–
BSW	CTD10-01	72.5	0.104	28.0	0.0	0.0	0.0	0.0	0.0	–	0.0	–	–	2.3[c]	0.3[b]	0[a]	-0.1[a]
E2-West																	
Flange	445-17ROV 03F	61.2	2.12	25.4	12.1	61.8	bdl	0.66	bdl	nd	1.59	bdl	bdl	3.40	-10.8	-0.3	-2.3
E2- South																	
Iced Bun	446-20ROV 07F	47.5	15.0	2.56	570	1301	8.67	59.5	3.3	4.0	48.9	-7.6	-99.9	8.10	-3.7	0.6	-1.2
Dog's Head	446-20ROV 10F	59.4	14.1	6.12	856	1450	8.04	36.0	4.0	6.7	25.6	-7.0	-98.7	10.4	-4.4	0.3	-1.6
E2-South[a]																	
Dog's Head[a]	JC42-132-Y1-07	42.8	17.2	3.7	1387	2075	nd	nd	6.9	nd	nd	nd	nd	nd	nd	1.2	1.8
Sepia[a]	JC42-135-Y2-04	38.8	21.2	1.9	1003	2034	nd	nd	6.8	nd	nd	nd	nd	nd	nd	0.9	-0.2
Sepia Flange[a]	JC42-132-B1-02	40.2	4.06	3.6	748	2095	nd	nd	6.5	nd	nd	nd	nd	nd	nd	0.9	-0.6

mM, mmol/L fluid; µM, µmol/L fluid; nM, nmol/L fluid; mm, mmol/Kg fluid; nd, not determined; bdl, below detection limits; LOQ, Limit of quantification; T_{MAX}, maximum temperature measured; BSW, Bottom seawater; Na_{Meas}, Na measured; Na_{CB}, Na charge balanced (see text).

pH_{MIN} = lowest pH measured at 25°C; pH (in situ) = pH at measured temperature and 250 bar.

a, Data from James et al. (2014); b, data from Craig (1970); c, data from Reeves et al. (2011).

consisted of nine injections of 7 µL each and the result is an average of the last three injections out of nine. The isotope ratios were normalized to VSMOW seawater material. For water isotopes the analytical uncertainties are ~0.09‰ and ~0.25‰ for $\delta^{18}O_{H2O}$ and δD_{H2O}, respectively.

Stable carbon and hydrogen isotope ratios ($^{13}C/^{12}C$ and $^2H/^1H$) of CH_4 and CO_2 were determined using GC-isotope ratio mass spectrometry (GC-IRMS) at MARUM as detailed in Pape et al. (2020a). CH_4 and CO_2 were separated by gas chromatography. Subsequently, CH_4 was either combusted (1,030°C) or pyrolyzed (1,440°C) to generate CO_2 or H_2, respectively. CO_2 or H_2 were then transferred to the IRMS for analysis of $^{13}C/^{12}C$ or $^2H/^1H$. All gas samples were injected at room temperature by manual syringe injection. Reported isotope ratios are arithmetic means of at least triplicate measurements and are given in the δ-notation relative to Vienna Pee Dee Belemnite (VPDB) and Vienna Standard Mean Ocean Water (VSMOW; for carbon and hydrogen, respectively). Reproducibility was proved using commercial CH_4 and CO_2 standards (Isometric Instruments, Canada; Air Liquide GmbH, Germany). Standard deviations of triplicate stable isotope measurements were <0.5‰ ($\delta^{13}C_{CH4}$). Because CH_4 concentrations were below the calibrated range of the GC-IRMS at the MARUM, samples were re-analysed for $\delta^{13}C_{CH4}$ by GC–IRMS at GEO-data Gesellschaft für Logging-Service mbH, Germany (see Pape et al., 2020b).

Sulphur isotopes ($\delta^{34}S_{H2S}$) were measured using an EA-IRMS (elemental analyser isotope ratio mass spectrometry) using a Flash EA isolink interfaced to a ThermoFisher Scientific Data V Advantage mass spectrometer. Analysis was conducted at the Institute of Geology and Palaeontology at the University of Münster. Results are reported in the δ-notation relative to Vienna Canon Diablo Troilite (VCDT). Reproducibility of the measurement was determined by replicate measurements and was better than ±0.3‰. Analytical performance was monitored using international reference materials IAEA S1, S2, S3 and NBS 127 as well as lab internal standards.

Analytical Methods: Fluid Inclusions

Microthermometry was carried out on anhydrite-hosted fluid inclusions from a chimney sample at the vent orifice of Dog's Head. A Linkam heating/freezing stage in combination with a LNP2 flow regulator and a Zeiss Axioskop was used to observe phase transitions in two-phase liquid-vapour fluid inclusions. The temperature of the heating/freezing stage was calibrated using FLINC® synthetic fluid inclusions hosted in quartz. Phase transitions in the H_2O system (freezing point: 0.0°C, critical temperature: 374.1°C) were used to calibrate the temperature sensor of the Linkam stage. The calibration procedure yielded temperatures of -0.1°C and 373.4°C for the freezing point and critical temperature, respectively. These values agree with the range of 15 long term control measurements of 0.04 ±0.07°C and 373.6 ±0.75 °C and show that the temperature sensor provided accurate and precise temperatures. Both accuracy and precision are within ±0.1°C at temperatures around the freezing point of pure H_2O and are better than ±1°C in the high-temperature regime (>>100°C).

Calculation of Endmember Composition

Sampled hydrothermal vent fluids inadvertently contain a fraction of seawater that was entrained naturally in the subseafloor immediately prior to sampling or accidently during sampling, due to the dead volume of the inlet snorkel. This typically results in a two-component mixture of seawater and hydrothermal fluid. We have used the Mg concentrations in the vent fluid samples at E2-S and E2-W to calculate the chemical composition of hydrothermal endmember solution for all elements by extrapolating to zero Mg.

Endmember temperatures were calculated using isenthalpic-isobaric mixing, by considering a temperature and salinity-dependent heat capacity of the fluid. This dependence of salinity and temperature was calculated using the scheme by Driesner (2007), which calculates the thermodynamic data of H_2O-NaCl fluids using thermodynamic data of pure water (Haar et al., 1985).

Salinities and Entrapment Temperatures (T_e) in Fluid Inclusions

Fluid inclusions in hydrothermal precipitates can be used for tracing salinity and temperature in hydrothermal fluids. When crystals grow from hydrothermal solutions, they tend to incorporate microscopic volumes of the hydrothermal fluid, called fluid inclusions. The study of phase-transitions in these inclusions allows for the reconstruction of physio-chemical conditions in active and fossil hydrothermal systems (Peter and Scott, 1988; Xu, 2000; Baker and Lang, 2001; Bieseler et al., 2018; Diehl et al., 2020a). Measurements of ice-melting temperatures (T_m) and homogenization temperatures (T_{hom}) in two-phased fluid inclusions enable the calculation of salinities and entrapment temperatures (T_e) (Vityk et al., 1994). Both measurements represent the properties of the hydrothermal fluid during crystal growth if the inclusions have not changed in composition or volume since they were incorporated (Roedder, 1984; Bodnar, 2003) they provide key information on temperature and salinity of hydrothermal fluids during crystal growth. Fluid inclusions in anhydrite are known to re-equilibrate easily and may increase in volume (stretching) during the microthermometric measurement itself. We used the procedure proposed by Vanko and Bach (2005) to avoid inclusions being affected by stretching.

Using thermodynamic relationships in the H_2O-NaCl system, salinities were calculated from ice-melting temperatures (T_m) while entrapment temperatures (T_e) were calculated from the homogenization temperatures (T_{hom}) and salinities using empirical relationships (Vityk et al., 1994; Atkinson, 2002). The uncertainties in the determination of these two parameters is based on the uncertainty of the temperature determination during the microthermometric work. The accuracy and precision are ±0.1°C and ±1°C for the freezing point and the homogenization temperature (T_{hom}) determinations, respectively, and result in maximum uncertainties of <±0.2 wt.% NaCl eq. and <±2°C for entrapment temperatures (T_e). The pressure correction for entrapment at seafloor conditions (250 bar) corresponds to a 15-17°C adjustment.

Thermodynamic Modelling

The use of IGTs facilitated the measurement of concentrations of gases dissolved in the fluids, and hence the reconstruction of *in-situ* pH and redox, which are key parameters controlling speciation of elements and solubility of minerals in the hydrothermal fluids prior to venting. The H_2 and H_2S concentration data were plotted in activity-activity plots, constructed using the R based software package CHNOSZ (Dick, 2019). We assumed unity activity coefficients for both gases.

Sub-surface processes in hydrothermal systems can be examined using thermodynamic reaction-path models. Reaction-path models were constructed using the Geochemists Workbench™ (GWB) software package and a tailor-made 400 bar database assembled by SUPCRT92 (Johnson et al., 1992). For these models, measured bottom seawater (BSW) was heated to hydrothermal temperatures while allowing minerals to precipitate. Using the REACT module of GWB, the heated fluid was then allowed to react with the host rock till the fluid became rock-buffered i.e., attained quartz saturation. Host rock data for samples taken in close vicinity to the vent sites (Sample ID: WX.30, 29, 28, 27, 2 & 1) were utilized from Leat et al. (2000). All major elements were considered for the reaction path models (except P). Ba, Cu and Zn concentrations were formally recalculated and added to the system as barite, chalcopyrite, and sphalerite.

Catabolic energy landscape computations were carried out as described in Amend et al. (2011). The REACT module of GWB was used along with a 250 bar database assembled using SUPCRT92 (Johnson et al., 1992) to simulate mixing of cold BSW with hot hydrothermal fluid represented by the Iced Bun site endmember composition. Minerals were not allowed to precipitate during mixing and redox reactions were also suppressed. Acid-base reactions were allowed to equilibrate. For this model 8 catabolic reactions were considered (**Table 2**). Five of the reactions represented aerobic respirations using different inorganic electron donors and three denoted anaerobic respiration.

Values of Gibbs energy (ΔG_r) for catabolic reactions were computed using the relation:

$$\Delta_r G = \Delta_r G^o + RT \ \ln Q_r$$

where $\Delta_r G^o$ denotes the standard Gibbs energy of reaction, R and T represent the gas constant and temperature in Kelvin,

respectively, and Q_r stands for the activity product of reaction r, which is evaluated with the relation.

$$Q_r = \prod a_i^{v_{i,r}}$$

where a_i denotes the activity of species i raised to the stoichiometric reaction coefficient $v_{i,r}$. The B-dot equation was used to calculate activity coefficients needed to convert species concentrations to activities. The Q-term accounts for the chemical composition of the mixed hydrothermal fluid, it also accounts for intracellular concentrations for building blocks of cells. Values of $\Delta_r G^o$ were calculated at 250 bar and the temperatures of interest with the computer code SUPCRT92 (Johnson et al., 1992), which relies on the relation of

$$\Delta_r G^o = \sum v_{i,r} \Delta_a G_i^o$$

where $\Delta_a G_i^o$ represents the apparent standard Gibbs energy of formation of the ith species in reaction r.

For catabolic reactions the amount of energy available was then calculated as a function of either temperature or mixing ratios. This was done by multiplying the calculated Gibbs energy for the reaction at each temperature with the concentrations of reactants (in the mixed fluid). The stoichiometry of the reaction and the reactant present in limiting supply were taken into account and then multiplied with the amount of mixed fluid at that specific temperature (McCollom, 2007; Amend et al., 2011).

RESULTS

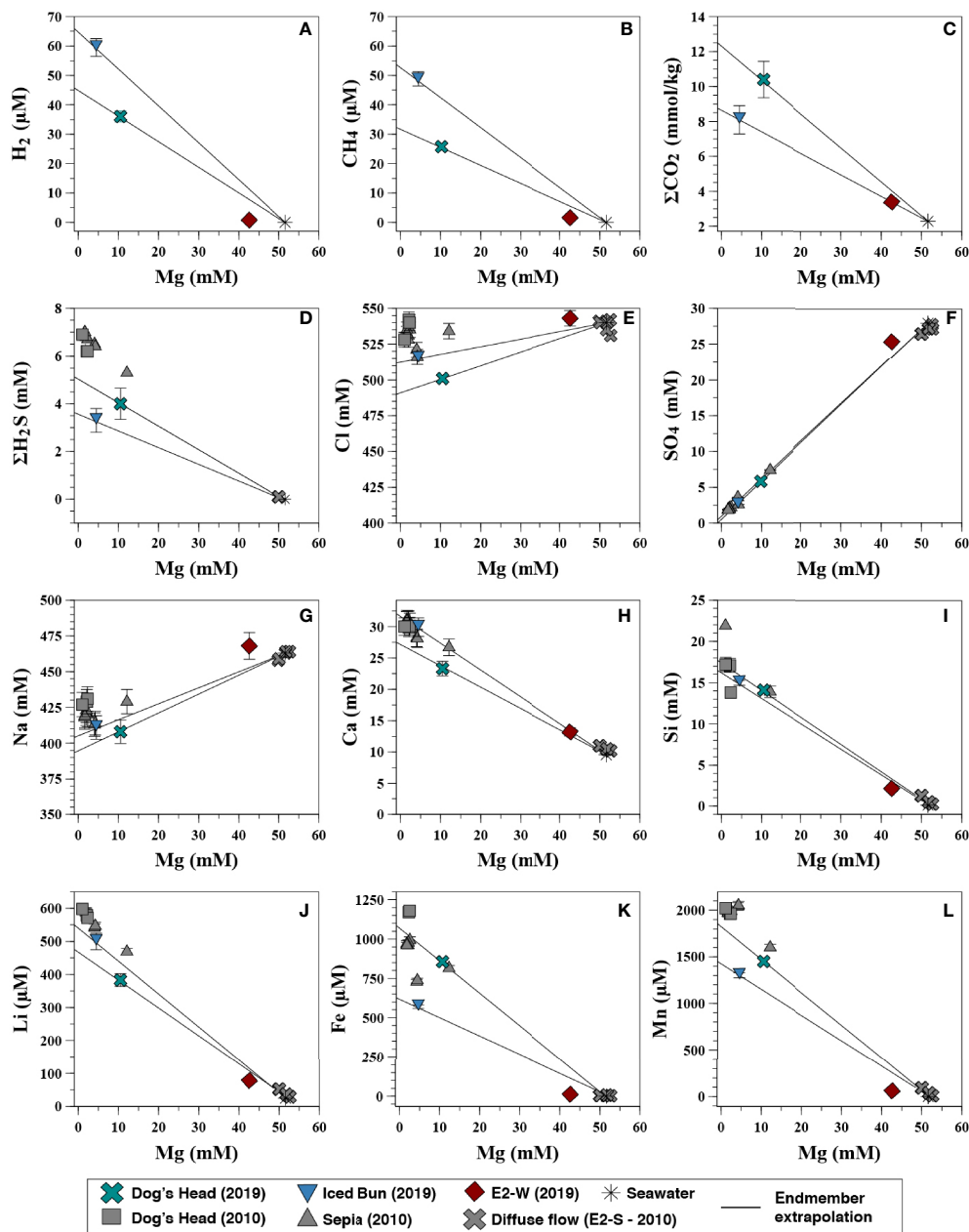## Temperature, pH, and Mg Contents

Focused venting of black smoker-type fluids at Dog's Head and Iced Bun in the E2-S area took place at maximum temperatures of 344°C and 320°C, respectively (**Table 1**). The fluids have a measured pH $_{(25°C, 1bar)}$ of 3.3 at Iced Bun and 3.2 at Dog's Head. Calculated pH $_{(in-situ)}$ values for these fluids were 4.8 for Iced Bun and 5.3 for Dog's Head (**Table 1**). Isenthalpic-isobaric mixing models indicate endmember temperatures of 386°C and 342°C for Dog's Head and Iced Bun, respectively (**Supplementary Figure 1**). These temperatures are accurate if all the Mg measured was contributed from entrainment of ambient seawater upon sampling.

The fluid at E2-W was characterized by a maximum measured temperature of 53°C (**Table 1**) and a relatively high Mg concentration (42.6 mM). An isenthalpic-isobaric mixing model indicates an endmember temperature of 273°C (**Supplementary Figure 1**). The fluid had a pH $_{(25°C)}$ of 6.7 and a pH $_{(in-situ)}$ of 6.6 (**Table 1**).

Dissolved Gases

The dissolved gases investigated in the fluids at E2-S (H_2, H_2S, CO_2 and CH_4) show variable concentrations and isotopic compositions (**Table 1**). The fluids at Dog's Head and Iced Bun have endmember H_2 concentration of 45.2 and 65.1 μM, respectively (**Figure 4A**). Endmember concentrations of CO_2 are 8.65 and 12.5 mM, respectively. CH_4 concentrations are 32.0 μM

TABLE 2 | Inorganic redox reactions.

Aerobic sulphide oxidation (ASO)	$H_2S + 2O_2 \rightarrow SO_4^{2-} + 2H^+$ (1)
Aerobic methane oxidation (AMO)	$CH_4 + 2O_2 \rightarrow CO_2 + 2H_2O$ (2)
Aerobic iron oxidation (AFeO)	$4Fe^{2+} + O_2 + 10H_2O \rightarrow 4Fe(OH)_3 + 8H^+$ (3)
Aerobic manganese oxidation (AMnO)	$6Mn^{2+} + O_2 + 10H_2O \rightarrow 6MnO_2 + 20H^+$ (4)
Aerobic hydrogen oxidation (AHO)	$2H_2 + O_2 \rightarrow 2H_2O$ (5)
Hydrogenotrophic sulphate reduction	$4H_2 + SO_4^{2-} + 2H^+ \rightarrow H_2S + 4H_2O$ (6)
Hydrogenotrophic methanogenesis	$4H_2 + CO_2 \rightarrow CH_4 + 2H_2O$ (7)
Anaerobic oxidation of methane (AOM)	$CH_4 + SO_4^{2-} + 2H^+ \rightarrow CO_2 + H_2S + 2H_2O$ (8)

All compounds represent aqueous species. $Fe(OH)_3$ represents ferrihydrite.

FIGURE 4 | Concentrations of dissolved volatiles, major and minor elements in the fluids recovered from E2 in 2019 (coloured) v/s Mg concentrations of the hydrothermal fluids. Concentrations of fluids sampled in 2010 by James et al. (2014) (Grey) are shown for comparison. The solid lines indicate linear regression to endmember composition. The analytical error bars are shown or are smaller than the symbols. **(A)** H_2 vs Mg, **(B)** CH_4 vs Mg, **(C)** CO_2 vs Mg, **(D)** H_2S vs Mg, **(E)** Cl vs Mg, **(F)** SO_4 vs Mg, **(G)** Na vs Mg, **(H)** Ca vs Mg, **(I)** Si vs Mg, **(J)** Li vs Mg, **(K)** Fe vs Mg, **(L)** Mn vs Mg.

at Dog's Head and 53.5 µM at Iced Bun (**Figures 4B, C**). The endmember fluids at E2-S have $\delta^{13}C_{CO2}$ values of -4.1 and -5.6‰ (**Table 3A**) and $\delta^{13}C_{CH4}$ values of -7.0 and -7.6‰. H_2S concentrations in the endmember fluids are 3.3 and 4.0 mM (**Figure 4D**) and $\delta^{34}S_{H2S}$ values are between +4.0 and +6.7‰.

The endmember concentrations for H_2 and CH_4 at E2-W were 3.75 and 9.03 µM, respectively (**Figures 4A, B**). The H_2S

concentration in this fluid was below the detection limit (<0.2 µM). The CO_2 endmember concentration is 8.55 mM (**Figure 4C**). These concentrations of dissolved gases at E2-W are lower than that at E2-S. The $\delta^{13}C_{CO2}$ value of -10.8‰ is lower than for the fluid at E2-S. Endmember values were not calculated for $\delta^{13}C_{CO2}$ due to processes affecting the CO_2 concentrations of the fluid in the mixing zone (cf. Formation of fluid at E2-West).

Other Dissolved Species

The high-temperature fluid feeding E2-S is depleted in Cl by ~9% relative to seawater with the lowest Cl endmember measuring 491 mM (**Figure 4E**). Sulphate is depleted in the Iced Bun and Dog's Head fluids with endmember concentration of ≤1 mM (**Figure 4F**). The Na_{CB} (Na calculated based on charge balance of the endmember) endmember concentration is depleted by ~10% relative to seawater (**Figure 4G**). Endmember Ca concentrations in the fluids are 31.8 and 26.8 mM (**Figure 4H**). Endmember Br and F is depleted relative to seawater with 809 – 754 µM and 47.5 - 59.4 µM, respectively (**Table 3A**). Endmember Sr concentrations show both, depletion and enrichment relative to seawater at Dog's Head and Iced Bun, respectively (**Table 3A**). The endmember concentrations of alkali metals K, Li, Rb and Cs (33.7 – 35.1 mM, 383 – 545 µM, 52.6 – 55.7µM, 468 – 538 nM) are higher than those of seawater (**Table 3A**).

Fluids sampled at E2-W have seawater-like concentrations of Na, Cl and Br. Endmember concentrations of K, Ca and Li are 29.3 mM, 30.2 mM and 328 µM, respectively, and are like endmember E2-S concentrations. However, SO_4, F and Si have endmember concentrations of 13 mM, 8.36 µM and 11.5 mM, respectively. These concentrations are markedly different from the endmember concentrations of the E2-S fluids.

The K/Cl, Sr/Cl, Li/Cl, Cs/Cl, Rb/Cl and Br/Cl are elevated in the fluids venting at E2-S and E2-W, except for Br/Cl at E2-W, which is seawater-like (**Table 4**). F/Cl ratios in all fluids are lower than in seawater. The E2-S element-to-Cl ratios measured in this study show deviations to those reported by James et al. (2014) (**Table 4**). Dog's Head fluids have lower Ca/Cl, K/Cl, Sr/Cl, Li/Cl, Cs/Cl and Br/Cl ratios than those sampled in 2010, whereas Na_{CB}/Cl ratios are slightly higher compared to the 2010 ratios.

E2-S endmember fluids are characterized by concentrations of Fe and Mn of 624 – 1074 µM and 1424 – 1821 µM, respectively. The metal concentrations in the endmember fluids from E2-S are lower than in the endmembers calculated from the 2010 samples (**Figures 4K, L**). E2-W has an endmember Fe and Mn concentrations of 69.0 and 351 µM (**Table 3A**; **Figures 4K, L**).

The total endmember REE (ΣREE) concentrations in the fluids from E2-S are 27 nmol/kg and 29 nmol/kg at Iced Bun and Dog's Head, respectively (**Table 3B**). Chondrite-normalized REE_N distribution pattern shows the characteristic light REE (La-Nd) enrichment and a positive Eu anomaly (Douville et al., 1999; Douville et al., 2002; Craddock et al., 2010, **Figure 5**).

Stable Oxygen and Hydrogen Isotopes

The $\delta^{18}O_{H2O}$ endmember value of +0.4 and +0.6‰ for fluids from E2-S are ^{18}O-enriched compared to the endmember ratio for the fluid sample at E2-W (-1.7‰, **Table 3A**). The δD_{H2O} values for all fluids are lower than seawater, with the lowest values in the fluid at E2-W (-2.3‰). The endmember δD_{H2O} and $\delta^{18}O_{H2O}$ values recorded in this study are lower than those of the fluids sampled in 2010 (**Table 3A**).

Fluid Inclusions

Microthermometry of 26 fluid inclusions was conducted in anhydrite precipitates from a chimney sample of Dog's Head (**Supplementary Table 1**). Two fluid inclusion types were identified during the investigation: Inclusion *Type I* is single phased and was not analysed. Inclusion *Type II* contains two-phases, with vapour-liquid inclusions and can be subdivided into *Type IIa* (<50 vol.% vapour) and *Type IIb* (≥50 vol.% vapour). *Type IIa* is the dominant inclusion type with 22 out of 26 measured inclusions. The remaining of 4 inclusions is classified as *Type IIb*. All *Type II* inclusions exclusively homogenize into the liquid phase suggesting a similar origin. T_m (ice-melting temperature) in individual inclusions ranged from -1.6 to -2.1°C. The corresponding calculated salinities range between 2.7 wt.% NaCl eq. (minimum) and 3.6 wt.% NaCl eq. (maximum). The average T_m of -1.8°C corresponds to a mean salinity of 3.1 wt.% NaCl eq., just slightly below seawater, for all inclusions. Calculated salinities (mean) for different inclusion types (*Type IIa* and *Type IIb*) are 3.1 and 3.2 wt.% NaCl eq. According to measured salinities, the inclusions can be grouped into two populations (**Supplementary Figure 3A**): 9 inclusions were determined to contain fluids with salinities significantly below seawater (<3.0 wt.% NaCl eq.) and 22 inclusions contained fluids with near-seawater salinities (3.0-3.6).

T_{hom} were determined between 211°C and 316°C (**Supplementary Figures 3B, C**). The calculated T_e range between 226-333°C with 9 of 22 T_e determinations above 300°C. The highest T_e was determined as 333°C, just 11°C lower than the measured temperature of 344°C during fluid sampling. Both these temperatures are significantly below the boiling temperature of 386°C at seafloor pressure.

DISCUSSION

The high-temperature fluids at E2-S have low Mg and SO_4 concentrations typical for black smoker type vent fluids. They are enriched in dissolved gases (CO_2, H_2, CH_4 and H_2S) and are depleted in Cl relative to seawater values. The fluids are enriched in alkalis, alkaline earth and transition metals as a result of high-temperature fluid-rock interactions in the sub-surface. Furthermore, the fluids have high Na/Cl and low Ca/Cl ratios and lower concentrations of Li, Rb, and REEs than the fluids sampled in 2010 (Cole et al., 2014; James et al., 2014). The low-temperature fluid sampled at E2-W have lower concentrations of dissolved gases, alkalis, alkaline earth, and transition metals than the fluid at E2-S. The high Mg and SO_4 contents of E2-W fluid indicates sub-surface mixing with entrained seawater.

In the following discussion we present evidence for the temporal variation of the E2 vent field, provide evidence for a single sourced fluid feeding the E2 system and imply the depth of the root zone as well as phase separation processes. We discuss the origin of dissolved gases at E2 by magmatic degassing and constrain sinks for the gases both in terms of abiotic and biotic processes taking place in the sub-surface. Important catabolic

TABLE 3A | Endmember concentrations and isotopic compositions of aqueous species from fluids recovered from E2-South and E2-West hydrothermal vent fields.

| Edifice	T_{max} [°C]	T_{calc} (C)	pH_{MIN} (25°C)	Na_{Meas} mM	Na_{CB} mM	K mM	Li µM	Rb µM	Cs nM	Ca mM	Sr µM	Cl mM	Br µM	F µM	Si mM	SO_4 mM	Fe µM	Mn µM	Al µM	H_2 µM	H_2S mM	CH_4 µM	CO_2 mm	$\delta^{13}C_{CO2}$ ‰	$\delta^{18}O$ ‰	δD ‰
BSW	0.5	–	7.7	460	463	10.0	25.1	1.26	2.0	9.56	82.6	540	820	72.5	0	28	0	0	0	0	0	0	2.3[c]	0.3[b]	0.0[a]	-0.1[a]
E2-West																										
Flange	53	273	6.7	nd	nd	29.3	328	32.5	351	30.2	96.1	nd	nd	8.36	11.5	13	69.0	351	–	3.75	0	9.03	8.55	nd	-1.7	-12.5
E2- South																										
Iced Bun	320	342	3.3	406	418	35.1	545	55.7	538	31.8	95.5	513	809	47.5	16.4	0	624	1424	9.50	65.1	3.61	53.5	8.65	-4.1	0.6	-1.2
Dog's Head	344	386	3.2	394	413	33.7	474	52.6	468	26.8	79.9	491	754	59.4	17.2	1	1074	1821	10.1	45.2	5.02	32.07	12.5	-5.6	0.4	-2.0
E2-South[a]																										
Dog's Head[a]	351	nd	3.0	435	nd	40.3	618	nd	618	31.5	105	536	842	39.1	17.7	0	1315	2106	nd	nd	6.7	nd	nd	nd	1.1	1.5
Sepia[a]	353	nd	3.1	426	nd	39.1	623	nd	623	32.5	105	532	838	38.4	22.6	0	1038	2116	nd	nd	7.6	nd	nd	nd	1.1	1.4
Sepia Flange[a]	313	nd	2.9	416	nd	38.0	604	nd	604	30.5	96.1	517	838	39.8	22.6	0	816	2280	nd	nd	7.1	nd	nd	nd	1.0	-0.8

TABLE 3B | Rare-earth element concentrations of the fluids from E2-S and E2-W hydrothermal vent fields.

Edifice	T_{max} [°C] (In situ)	Mg mM	La nM	Ce nM	Pr nM	Nd nM	Sm nM	Eu nM	Gd nM	Tb nM	Dy nM	Ho nM	Er nM	Tm nM	Yb nM	Lu nM	ΣREE nM
LOQ	-	-	0.0035	0.0013	0.0004	0.0036	0.0050	0.0002	0.0005	0.0004	0.0007	0.0005	0.0004	0.0001	0.0003	0.0002	-
BSW*100[d]	0	54.3	4.2	0.62	0.63	2.7	0.5	0.12	0.68	0.1	0.77	0.21	0.72	0.1	0.7	0.14	–
E2-West																	
Flange	53	42.6	bdl	bdl	bdl	bdl	0.68	0.41	bdl	bdl	bdl	bdl	0.05	nd	0.04	bdl	1.2
E2- South																	
Iced Bun	320	4.45	7.05	9.56	1.07	3.99	0.87	1.46	0.67	0.1	0.41	0.09	0.24	nd	0.2	0.03	26
		E.M	7.71	10.46	1.17	4.36	0.95	1.60	0.73	0.11	0.45	0.10	0.26	nd	0.22	0.03	27
Dog's Head	344	10.5	5.71	9.22	0.88	2.89	0.63	2.39	0.57	0.07	0.33	0.05	0.14	nd	0.10	0.01	23
		E.M	7.16	11.57	1.10	3.62	0.78	3.00	0.71	0.09	0.41	0.07	0.18	nd	0.12	0.02	29
E2-South[d]																	
Dog's Head[d]	351	1.02	6.28	11.6	1.36	5.26	1.06	1.27	1.61	0.19	0.56	0.09	0.21	0.02	0.13	0.01	30
	323	2.11	8.67	16	2	8.12	1.8	2.29	1.8	0.2	0.95	0.15	0.32	0.03	0.17	0.02	42
	323	2.28	8.06	17.4	2.2	9.14	2.06	1.88	1.9	0.23	1.1	0.17	0.37	0.03	0.19	0.02	45
		E.M	7.92	15.5	1.9	7.75	1.7	1.87	1.61	0.19	0.9	0.14	0.31	0.03	0.17	0.02	40
Sepia[d]	347	1.61	6.58	11.9	1.34	5.1	0.97	1.21	0.98	0.11	0.53	0.08	0.2	0.02	0.11	0.015	29
		E.M	6.8	12.2	1.38	5.25	1.01	1.25	0.98	0.11	0.55	0.09	0.2	0.02	0.12	0.01	30

mM, mmol/L fluid; µM, µmol/L fluid; nM, nmol/L fluid; mm, mmol/Kg fluid; nd, not determined; bdl, below detection limits; LOQ, Limit of quantification; T_{MAX}, maximum temperature measured; BSW, Bottom seawater; Na_{Meas}, Na measured; Na_{CB}, Na charge balanced (see text).

pH_{MIN} = lowest pH measured at 25°C and 1 atm; pH (in situ) = pH at measured temperature and 400 bar.

a, Data from *James et al. (2014)*; b, data from *Craig (1970)*; c, data from *Reeves et al. (2011)*; d, data from *Cole et al. (2014)*.
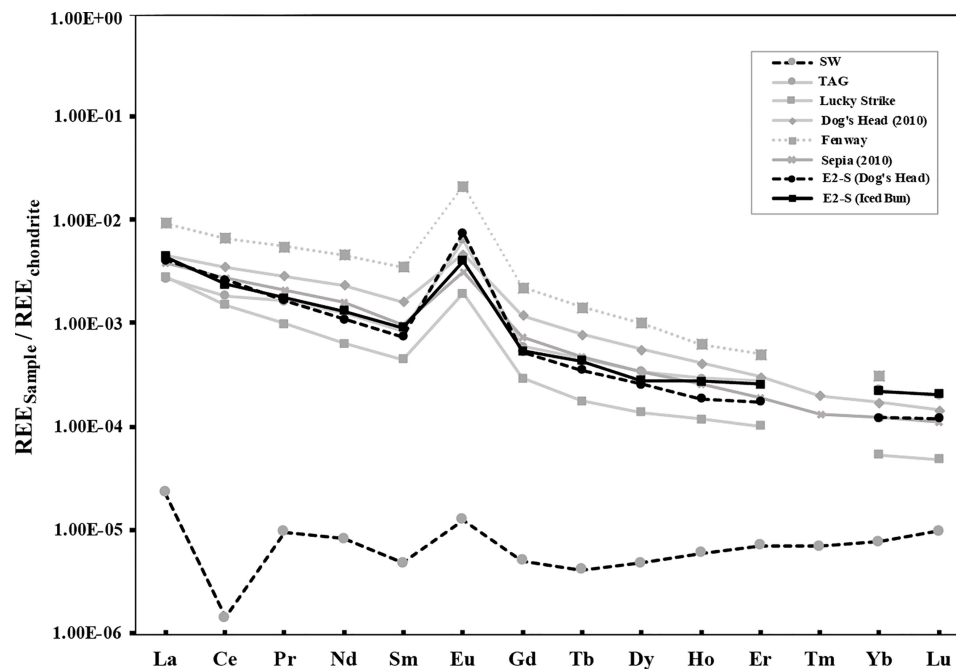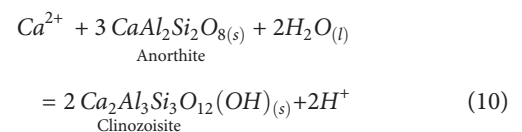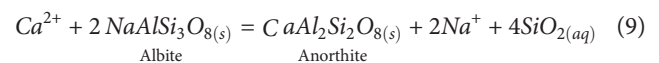
FIGURE 5 | Chondrite normalized REE pattern for endmember fluids from East Scotia ridge (Dog's Head and Iced Bun) compared with endmember fluids from other mid-oceanic ridge systems and back-arc basins that show similar patterns. The data represented here is from Douville et al. (1999) (TAG and Lucky Strike), Cole et al. (2014) (Dog's Head, Sepia), Craddock et al. (2010) (Fenway). The seawater (SW) values are taken from Cole et al. (2014).

reactions responsible for supporting the chemosynthetic ecosystem at E2 are also discussed.

Fluid Mineral Equilibria

Chloride is the dominant anion in hydrothermal fluids, it ranges in concentration due to phase separation and plays a key role in complexing dissolved metals. Hydrothermal vent fluids commonly show a tight correlation between the concentrations of cations and chloride. Metal concentrations in vent fluids can therefore be normalized to Cl for a comparison of fluids affected by different degrees of phase separation. It is known that partitioning of cations in the low-salinity fluid and the brine phase is not uniform during supercritical phase separation. Thus Cl normalization allows a better understanding of the dissolved species (**Table 4**, Berndt and Seyfried, 1990; Foustoukos and Seyfried, 2007a). Na/Cl and Ca/Cl ratios at E2-S are in the range for unsedimented mafic-hosted hydrothermal systems (Gallant and Von Damm, 2006; McDermott et al., 2018; Diehl and Bach, 2020b; Diehl and Bach, 2021). E2-W has a seawater like Na/Cl and Ca/Cl ratios, which are a result of excessive mixing of hydrothermal fluid with seawater. Theoretical studies and laboratory experiments have shown that thermodynamic equilibrium between plagioclase and epidote solid solutions in basalt hosted hydrothermal systems control the Na and Ca concentrations of the fluids (Berndt et al., 1989; Seyfried et al., 1991; Berndt and Seyfried, 1993; Seyfried and Ding, 1995). Higher temperature conditions favour the stability of anorthite, clinozoisite of the plagioclase and epidote solid solutions respectively, due to the following reactions:

$$Ca^{2+} + 2\ NaAlSi_3O_{8(s)} = C\ aAl_2Si_2O_{8(s)} + 2Na^+ + 4SiO_{2(aq)} \quad (9)$$
$$\underset{\text{Albite}}{} \qquad \underset{\text{Anorthite}}{}$$

$$Ca^{2+}\ + 3\ \underset{\text{Anorthite}}{CaAl_2Si_2O_{8(s)}} + 2H_2O_{(l)}$$

$$= 2\ \underset{\text{Clinozoisite}}{Ca_2Al_3Si_3O_{12}(OH)_{(s)}} + 2H^+ \quad (10)$$

These reactions result in Ca fixation and decrease in Ca/Cl ratios in hydrothermal systems. The Na/Cl ratios are lower and the Ca/Cl ratios are higher than seawater, indicating that albitization and Ca-release occur in the root zone of E2-S. However, in 2019 the fluids at Dog's Head had higher Na/Cl and lower Ca/Cl ratios than in 2010 (**Table 4**). This may indicate a subtle switch to less albitization and more Ca fixation. Likewise, the Li/Cl and Cs/Cl ratios were noticeably lower in 2019 than in 2010. These ratios are proxies for water/rock mass ratios (w/r). Field and experimental data have shown that alkalis are highly fluid mobile and get leached from basalt during fluid-rock interactions at high temperatures (Mottl and Holland, 1978; Seyfried et al., 1984; Von Damm et al., 1985a; Von Damm, 1990). The high mobility results in higher concentrations of dissolved alkalis in the fluids that have interacted with large masses of rock (**Table 3A**). Assuming that Li, Rb and Cs are fully leached from the rocks in the root zone w/r ratios can be calculated (e.g., Von Damm et al., 1985a). The glassy lava from the E2 segment contains ca. 0.15 ppm of Cs, ca. 8 ppm of Rb (Leat et al., 2000). Basaltic andesites commonly contain ca. 8 ppm of Li (Ryan and Langmuir, 1987). Using endmember compositions for

TABLE 4 | Molar element/Cl ratios for fluids from ESR. E2-West ratios are calculated from measured concentrations, while E2-S are calculated from EM values.

Edifice	Na_{CB}/Cl	Ca/Cl	K/Cl	Sr/Cl x10^{-3}	Li/Cl x10^{-3}	Rb/Cl x10^{-3}	Cs/Cl x10^{-3}	Br/Cl x10^{-3}	F/Cl x10^{-3}	Fe/Cl x10^{-3}	Mn/Cl x10^{-3}	Fe/Mn	Sr/Cl x10^{-3}
BSW	0.86	0.02	0.02	0.15	0.05	0.002	0.004	1.52	0.13	0.00	0.00	–	8.64
E2- West													
Flange	0.86	0.02	0.03	0.16	0.14	0.01	0.12	1.52	0.11	0.02	0.11	0.20	6.44
E2- South													
Iced Bun	0.82	0.06	0.07	0.19	1.06	0.11	1.05	1.58	0.09	1.22	2.78	0.44	3.00
Dog's Head	0.84	0.05	0.07	0.16	0.97	0.11	0.95	1.54	0.11	2.19	3.71	0.59	2.98
E2- South[a]													
Dog's Head[a]	0.80	0.06	0.07	0.19	1.12	nd	1.13	1.57	0.07	2.40	3.80	0.62	3.33
Sepia[a]	0.79	0.06	0.07	0.19	1.14	nd	1.12	1.58	0.07	1.90	3.90	0.49	3.24
Sepia Flange[a]	0.79	0.06	0.07	0.18	1.14	nd	1.15	1.62	0.08	1.50	4.30	0.36	3.14

BSW, bottom seawater; Na$_{CB}$, Na charge balanced (see text).
a = Data from James et al. (2014).

Li, Rb and Cs at E2-S and assuming 100% extraction of the elements the w/r ratios were ca. 2 for Cs and ca. 2 for Rb at both Iced Bun and Dog's head. The w/r ratios of ca. 2 for Iced Bun and ca. 3 for Dog's Head were calculated using Li. Moreover, the ratios in this study are higher compared to that calculated in 2010 (ca. 1.9) because of lower alkali abundances in these fluids.

Dog's Head and Iced Bun have very similar vent fluid compositions in terms of Na/Cl, K/Cl, Br/Cl, Si and predicted w/r ratios, indicating that the high-temperature fluids venting at E2-S are fed by a common root zone. Likewise, back in 2010, Dog's Head and Sepia had identical Na/Cl, K/Cl, Ca/Cl, Li/Cl and Cs/Cl which also points to a single sourced fluid at E2-S. We next discuss how the composition of the Dog's Head fluids has evolved between 2010 and 2019 and how this variation may indicate changes in the common root zone of the E2-S vents.

Temporal Variability of the E2 Vent Field

Continuous alteration of fresh rock over time can result in the loss of elements from the rock, thereby reducing the amount of fresh rock available for w/r interactions (high Na/Cl ratios). This results in higher w/r ratios and decrease in concentration of mobile elements. Higher Na/Cl ratios coupled with higher w/r ratios in 2019 as compared to 2010 provide evidence that the root zone at E2-S has undergone effective alteration over the duration of the past 9 years. Furthermore, the fluids sampled in 2019 have low δD_{H2O} and $\delta^{18}O_{H2O}$ compared to the fluids sampled in 2010 (**Table 3A**). While the low δD_{H2O} at E2 may be related to magmatic water input, the low $\delta^{18}O_{H2O}$ cannot be explained by this process (cf. Magmatic water input). The fluid sampled at Dog's Head in 2010 had an endmember $\delta^{18}O_{H2O}$ value of 1.1‰ while the fluid from 2019 has a lower value of 0.4‰. Hydrothermal alteration of the igneous crust by circulating seawater-derived fluids at high temperature will have the $\delta^{18}O_{H2O}$ values of the altered rocks decrease with time (Shanks, 2001 and references therein). The lower $\delta^{18}O_{H2O}$ values of the 2019 vent fluid may indicate that the rocks in the root zone are more altered, which is consistent with the higher w/r ratios derived from the decreased concentration of fluid mobile elements (Rb, Li).

Experimental work has shown that REE concentrations are also affected by the intensity of hydrothermal alteration: the REE concentrations decrease and the positive Eu anomaly becomes more pronounced as the extent of hydrothermal alteration of mafic rocks increase (Beermann et al., 2017). REE$_{CN}$ (chondrite normalised) pattern observed in the fluids from E2-S are typical for mature mafic hosted hydrothermal systems (**Figure 5**). ΣREE measured in this study is lower than 2010 (Cole et al., 2014). This decrease in total REE content would be consistent with an increased extent of rock alteration in the root zone. However, REE solubility in hydrothermal fluids is also controlled by temperature, pH and redox conditions during high-temperature fluid-rock interactions (Craddock et al., 2010). A lower temperature in the root zone could therefore also explain the observed drop in ΣREE.

Our fluid inclusion study provides insights into the temporal evolution of salinity and phase separation processes taking place at E2. The fluid inclusion data at E2-S show that the fluids salinity was either slightly lower than or close to that of seawater (**Supplementary Figure 3C**). Although the time of entrapment of these inclusions was not determined, the low salinity in most of the inclusions in the young top of the chimney sample provide evidence for low Cl venting fluid at E2 during the past years. In addition to the low Cl concentrations measured in the fluids in 2019 and 2010, the fluid inclusion salinities indicate that phase separation has been affecting fluid compositions at E2-S for a prolonged period, despite the apparent changes in the extent of alteration in the root zone.

In summary, the root zone of E2-S may have changed slightly towards a more altered basement and slightly lower temperatures, but it appears that the process of phase separation (supercritical) taking place at E2 is constant and has not changed significantly.

Depth of the Root Zone

The concentration of dissolved Si in hydrothermal vent fluids can be used to estimate the depth (pressure) and temperature in the hydrothermal root zone (Bischoff and Rosenbauer, 1985; Von Damm et al., 1991; Foustoukos and Seyfried, 2007c). This thermobarometer is calibrated for quartz which is commonly present in hydrothermally altered mafic rocks. Since quartz solubility is a function of temperature and pressure, either one can be estimated if the other one is known. Using this relation,

sub-surface conditions of fluid-quartz equilibration at E2-S was calculated (**Figure 6**). With the calculated endmember Si concentrations and the measured temperature at E2-S, the equilibrium pressure was calculated at ∼300 bar and ∼500 bar at Dog's Head and Iced Bun, respectively. Silica concentrations at Dog's Head in this study is slightly lower than in 2010. Silica concentration in the Sepia fluids was high (22.3 mM, James et al., 2014), corresponding to unreasonably high 800-900 bar pressure. James et al. (2014) argued that the root zone temperatures at 'Sepia' were probably higher than the measured 353°C and that cooling (but no quartz precipitation) in the upflow zone gave rise to the high apparent pressures. The low pressures (300- 350 bar in 2019) obtained for Dog's Head may indicate that quartz did precipitate. At Iced Bun, the estimated depth of quartz equilibria is 500 bar. It is highly unlikely that the depth of the hydrothermal root zone for vent orifices that are in such proximity [ca. 60 m of each other, Tyler, (2012)] have such a huge variability. More plausibly, the estimated pressures are an artefact of conductive cooling (James et al., 2014). When conductive cooling takes place, silica precipitation may or may not take place. The shallow pressures obtained for Dog's Head indicate some quartz precipitation in the upflow zone. In contrast, the high silica concentrations in the Sepia vent fluids in 2010 (James et al., 2014) indicate that quartz did not precipitate upon cooling. The effect of conductive cooling and quartz precipitation kinetics on the Si concentrations of the fluids makes it difficult to obtain a realistic depth of the reaction zone from quartz equilibrium pressures at E2-S.

Phase Separation

The high-temperature fluids venting at E2-S have a Cl concentration that is significantly lower than that of seawater. The lowest endmember concentration was 491 mM (**Figure 4E**). No major Cl sink is known to exist in mafic-hosted hydrothermal systems and therefore Cl depletions observed in such systems are typically attributed to phase separation (Von Damm, 1990; Von Damm, 1995; Foustoukos and Seyfried, 2007b). Seafloor pressure of ∼260 bar places the two-phase boundary at 386°C (**Supplementary Figure 2**; Driesner and Heinrich 2007), while the critical point of seawater is 407°C at 298 bars (Bischoff, 1991). Our investigation shows that the observed variability in salinities and temperatures in hydrothermal fluid samples and fluid inclusions cannot be produced by subcritical phase separation (**Supplementary Figure 3**). The Cl concentrations lower than seawater in the hydrothermal fluids at E2-S are therefore likely a result of phase separation at supercritical conditions. Subcritically phase separated fluids would produce mixing lines with considerably lower Cl concentrations when mixing with cold seawater. The temperature-salinity plane observed for fluid samples and inclusion data is characteristic for fluids produced by phase separation at pressures of at least over 300 bar. Elevated Br/Cl ratios at E2-S relative to seawater corroborate the idea of phase separation under supercritical conditions (cf. McDermott et al., 2018). Laboratory experiments have shown that Br partitions preferentially into the low salinity phase under supercritical
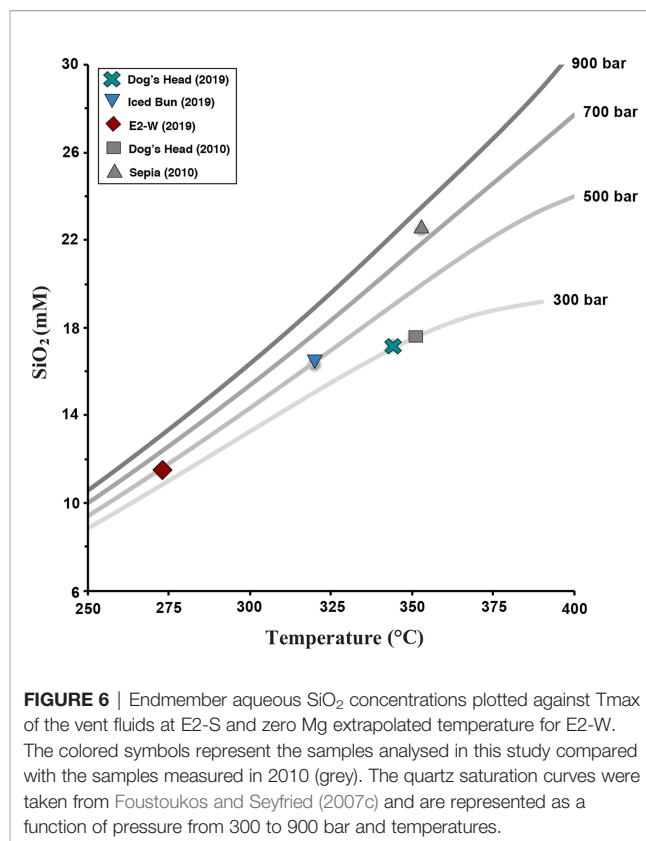
FIGURE 6 | Endmember aqueous SiO$_2$ concentrations plotted against Tmax of the vent fluids at E2-S and zero Mg extrapolated temperature for E2-W. The colored symbols represent the samples analysed in this study compared with the samples measured in 2010 (grey). The quartz saturation curves were taken from Foustoukos and Seyfried (2007c) and are represented as a function of pressure from 300 to 900 bar and temperatures.

conditions, resulting in increased Br/Cl ratios (Berndt and Seyfried, 1990; Foustoukos and Seyfried, 2007a). Using the Cl normalized partition coefficients and the following formula:

$$D_{\frac{Br}{Cl}} = \frac{\left(\frac{M_{Br}}{M_{Cl}}\right)_v}{\left(\frac{M_{Br}}{M_{Cl}}\right)_b} \tag{11}$$

where $\left(\frac{M_{br}}{M_{Cl}}\right)_v$ and $\left(\frac{M_{br}}{M_{Cl}}\right)_b$ represents the molal concentration of Br/Cl in the low salinity and high salinity phase, respectively (Berndt and Seyfried, 1990; Foustoukos and Seyfried, 2007a). It is known that vapour-brine partition coefficients for Br increases with decreasing fluid density and can be related with the following expression:

$$log\ D_{Br/Cl} = \ -13.04 - 54.95\ (log\rho_w) - 76.93\ (log\rho_w)^2 - 36.09(log\,\rho_w)^3 \tag{12}$$

where $p_w = density\ of\ pure\ seawater$ (Foustoukos and Seyfried, 2007a).

Endmember Br/Cl ratios at E2-S are 1.54 and 1.58 (**Table 4**), which are higher relative to seawater value of 1.52. These Br/Cl ratios give values of $D_{Br/Cl}$ of 1.01 and 1.04. Values of D >1 is known to be a result from the formation of a low salinity phase (Foustoukos and Seyfried, 2007a). Moreover, the calculated D values correspond to densities of ∼0.25 g/ml for the fluid at E2-S. This fluid density allows us to confine the conditions of phase separation to a pressure and temperature range of 320 to 390 bar and 420 to 450°C. The Cl-depleted nature of the fluids from E2-S

represents a supercritical phase separated fluid owing to their depleted Cl concentrations relative to seawater and density constraints (Bischoff and Pitzer, 1989; Bischoff, 1991). The cooler temperatures of 320 to 344°C measured at seafloor conditions suggest that the fluids have been undergoing conductive cooling prior to venting.

Phase separation is known to affect the concentrations of dissolved gases in hydrothermal fluids. Cl-depleted fluids have a higher concentration of dissolved gases relative to conjugate brine phases. This is also true for the fluids at E2-S. Fluids with low concentration of Cl show the highest concentration of CO_2 and H_2S (**Figures 4C–E**), while concentrations of dissolved H_2 and CH_4 do not show similar trends. CH_4 abundances likely represent a CH_4-Cl rich fluid (brine phase) mixing with the vapour rich fluid at E2-S.

Sub-Surface Processes and Consequences for Concentrations of Dissolved Metals and Gases

The pH of the fluid and metal-chloro complexes (under the effect of pressure and temperature) play a key role for the concentrations of dissolved metals in hydrothermal fluids. The temperatures required to have high concentrations of metals stable in seawater-like solutions decrease in the order Cu>Fe>Zn>Mn (Seewald and Seyfried, 1990). It is therefore expected that a cooled hydrothermal fluid will lose Cu and Fe by mineral precipitation faster than Zn and Mn. The fluids at E2-S have a relatively high endmember Mn concentration but low Fe concentrations (**Table 3A**). The low Fe/Mn ratios at E2-S (0.20 to 0.59) may represent the loss of Fe relative to Mn because of extensive conductive cooling of the fluid. To test this hypothesis, we applied the Fe/Mn geothermometer by Pester et al. (2012), derived from an empirical relation between the Fe/Mn ratios of hydrothermal fluids and temperature. The calculated temperatures (e.g., 305°C for Dog's Head) are lower than the measured temperatures (here: 344°C). The same applies for the Dog's Head fluids analysed in 2010 (**Table 3A**), which give Fe/Mn temperatures of 308°C (at measured 351°C). Sepia and Sepia Flange show even lower Fe/Mn ratios indicative of even more cooling-related Fe-precipitation there. These overall low Fe/Mn ratios are a clear indication that the fluids venting at E2-S undergo extensive cooling and pyrite precipitation prior to venting at the seafloor (**Figure 8**). The 40°C cooling of Sepia Flange relative to Sepia vent (James et al., 2014) come with a drop in Fe concentrations of >200 µM. The associated changes in H_2S concentrations (drop by 500 µM) and pH (drop from 3.1 to 2.9) are consistent with the idea of pyrite precipitation.

The low concentrations of dissolved H_2 in the fluids at E2-S (<1 mM) are typical for unsedimented mafic hosted hydrothermal systems (e.g., Welhan and Craig, 1983; Merlivat et al., 1987; Evans et al., 1988; Proskurowski et al., 2008; Diehl and Bach, 2020b; Diehl and Bach, 2021). Dissolved H_2 in hydrothermal fluids are known to be controlled as a result of fluid-mineral equilibria and phase separation processes, where H_2 abundances are buffered as a result of equilibration of Fe-bearing sulphide, oxides and aluminosilicate minerals (Seyfried

and Ding, 1995; Seyfried et al., 2003). Phase separation can also affect the concentration of dissolved gases such as H_2. Cl-depleted vapour phases are usually associated with high concentration of dissolved gases. However, phase separation alone at E2-S is likely unable to explain the concentration of H_2 in these fluids.

High-temperature fluid-rock interaction in the sub-surface root zone results in buffering the H_2 concentration of these fluids. Experimental basalt alteration studies have shown that pyrite-pyrrhotite-magnetite (PPM) and hematite-magnetite (HM) assemblages are predicted to exist in the range of redox conditions for natural hydrothermal systems (Seewald and Seyfried, 1990; Seyfried et al., 1991; Seyfried and Ding, 1995). The stability of these buffers can be predicted using thermodynamic data at various sets of temperature and pressure conditions. The known endmember H_2 concentrations for the fluids at Iced Bun and Dog's Head, predict H_2 concentrations that are consistent with the HM buffer at temperatures of ~358 and ~340°C at 300 bar (**Figure 7**). The higher degree of conductive cooling at Iced Bun relative to Dog's Head results in the offset of the data from the predicted HM buffer. The measured concentrations of H_2 at Iced Bun correspond to an equilibrium fluid temperature of ~358°C (**Figure 7**), while the fluid at Dog's Head is predicted to have a temperature of ~340°C. The fluid temperature predicted at Dog's Head are close to the measured temperatures of 344°C. The higher temperature predicted for fluids emitting at Iced Bun could be a result of addition of H_2 from rapid pyrite precipitation after equilibration with the HM buffer, during fluid upflow. However, we cannot rule out the fact that the fluid venting at Iced Bun underwent a higher degree of conductive cooling compared to Dog's Head, and therefore the H_2 concentrations could also be the result of higher equilibration temperatures (>320°C).

Endmember concentrations of dissolved H_2S of 3.61 and 5.02 mM in the fluids emitted at E2-S are within the known range of basalt-hosted hydrothermal systems (Diehl and Bach, 2020b; Diehl and Bach, 2021). $\delta^{34}S_{H2S}$ values of fluids from E2-S range from +4.0 to +6.7‰. Such $\delta^{34}S_{H2S}$ values have been previously reported from the Lau Basin (McDermott et al., 2015a). The H_2S in unsedimented basalt hosted hydrothermal systems can be either a result of mantle derived sulphide present in rocks in the form of pyrite and pyrrhotite with $\delta^{34}S_{H2S}$ values of +0.1 ±0.5‰ (Sakai et al., 1984) and/or reduced seawater SO_4, with a $\delta^{34}S_{H2S}$ value of +21.0 ±0.2 ‰ (Rees et al., 1978). At E2-S the $\delta^{34}S_{H2S}$ values are a result of mantle derived sulphur that varies from 81 and 69% relative to seawater derived sulphur of about 19 and 31% in these fluids.

Conductive cooling of fluids during ascend to the seafloor can result in pyrite precipitation, which can in turn affect the concentration of H_2, H_2S and Fe in the fluid (McDermott et al., 2018). Pyrite precipitation produces H_2 and acidity, while consuming dissolved Fe and H_2S:

$$Fe^{2+} + 2H_2S_{(aq)} = FeS_{2(s)} + 2H^+ + H_{2(aq)} \qquad (13)$$
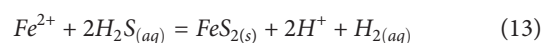
Indeed, the fluid venting at Iced Bun appears to be affected by pyrite precipitation as its fluid is characterized by low
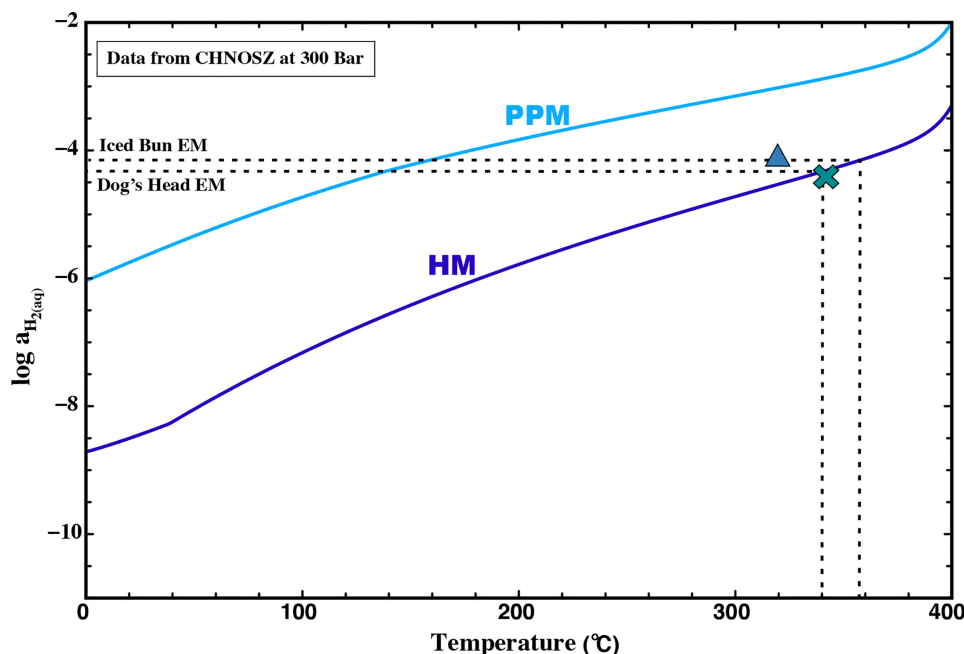
FIGURE 7 | Activity diagram showing aqueous H_2 abundances in equilibrium with pyrite-pyrrhotite-magnetite (PPM, blue line) and heamatite-magnetite (HM, purple line) at 300 bar and corresponding temperatures. The lines were drawn using thermodynamic data from CHNOSZ and references therein (Dick, 2019). Endmember H_2 concentrations and T_{max} for E2 is shown as Dog's Head (cross) and Iced Bun (triangle). The dashed line indicates endmember H_2 extrapolated to its associated temperature as a function of the HM buffer.

concentrations of Fe and H_2S, a higher concentration of H_2, and lower pH $_{(in-situ)}$ relative to Dog's Head (**Table 1**, **3A**). Fluid venting at Dog's Head could also be affected by pyrite precipitation in the subsurface (low Fe/Mn ratios), but it appears that the pyrite precipitation at Iced Bun is more pronounced than at Dog's Head. Activity-activity diagrams for H_2S and H_2 indicate that Dog's Head and Iced Bun plot near the hematite-magnetite-pyrite invariant point in the Fe-S-O-H system (**Figure 8**). Deviations from the invariant point can be accounted for by the facts that (1) the natural system is compositionally more complex than the Fe-O-H-S system for which the diagram is representative of and (2) there is considerable uncertainties in concentration-activity relations (Scheuermann et al., 2019). H_2S concentrations at E2-S may also have been influenced by phase separation, because Dog's Head fluid (low Cl) have higher concentration of H_2S than the high-Cl fluids venting at Iced Bun (**Table 3A**). As shown, the dissolved H_2 and H_2S concentrations at E2-S are mainly a result of fluid-mineral equilibria, but phase separation and cooling-induced pyrite precipitation are additional influences.

Dissolved Carbon Species

Elevated concentrations of dissolved CO_2 relative to seawater in BAB-hosted hydrothermal systems result from magmatic degassing (Takai et al., 2008; Reeves et al., 2011; Seewald et al., 2015; Seewald et al., 2019). However, a small fraction of CO_2 in the fluids could also result from leaching of CO_2 trapped in rocks as inclusions. Basaltic glasses from the ESR have a CO_2

concentration of <200 ppm (Mattey et al., 1984). Assuming a w/r of 2 (calculated for E2-S in this study), complete leaching of CO_2 from the rocks would contribute a CO_2 concentration of no more than 4 mmol/kg CO_2. Therefore, the higher abundances of dissolved CO_2 (**Figure 4C**) at E2-S are primarily a result of magmatic degassing with a minor possible contribution of CO_2 leached from basalts.

The carbon isotopic signatures of fluids from E2-S reveal endmember $\delta^{13}C_{CO2}$ values of -4.1 and -5.6‰, which are within the known range of BAB hosted hydrothermal system (Reeves et al., 2011; Seewald et al., 2015; Diehl and Bach, 2020b; Diehl and Bach, 2021). In contrast, basaltic glass at ESR has more negative $\delta^{13}C_{CO2}$ values of -15.0 to -19.9‰ (Mattey et al., 1984). Degassed CO_2 from basaltic melts at MOR have more positive $\delta^{13}C_{CO2}$ values, such as those at Lucky Strike hydrothermal system (-3.9 to -5.6‰) that are interpreted to reflect replenishing of the magmatic reservoir (Javoy et al., 1978; Mattey, 1991; Pester et al., 2012; Holloway and Blank, 1994). The high abundance and ^{13}C-enriched nature of CO_2 in the fluids at E2-S relative to the basaltic glass at ESR are likely a result of degassing from a magma reservoir that has undergone replenishment.

The endmember CH_4 concentrations (25.6 and 48.9 μM) are low relative to other BAB-hosted hydrothermal systems (Reeves et al., 2011; Seewald et al., 2015; Seewald et al., 2019). A variety of processes can contribute towards the CH_4 concentrations in hydrothermal systems that can range from abiotic sources, microbial activity and thermogenesis of sediments and/or organic matter (Von Damm et al., 1985b; Welhan, 1988;
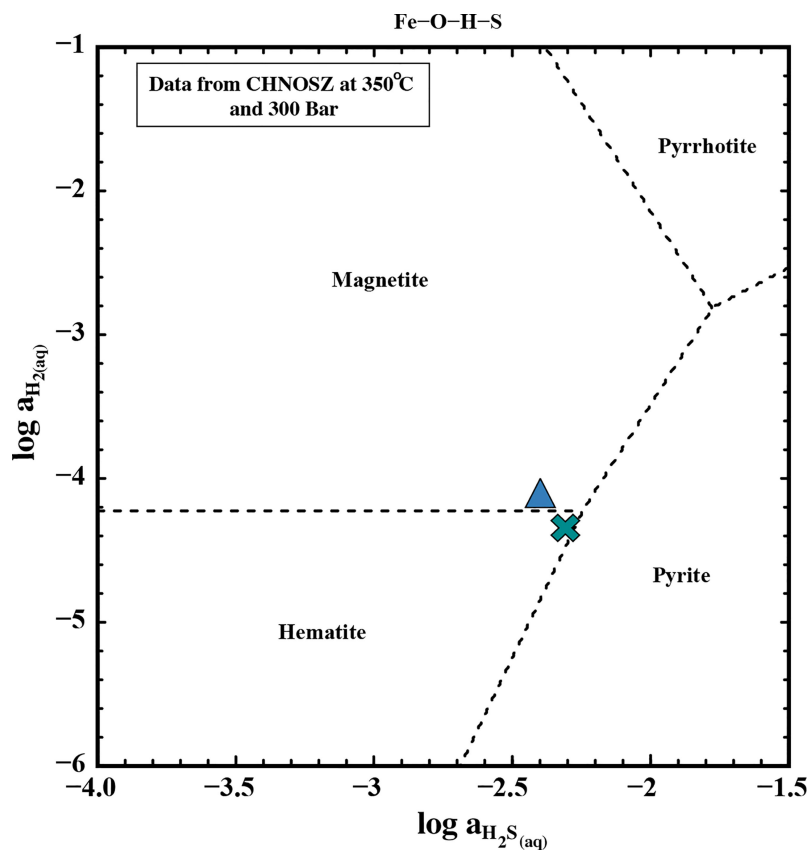
FIGURE 8 | Activity diagram showing the phase relations in a Fe-O-H-S system at 350°C and 300 bar. The data to plot the mineral fields were acquired using CHNOSZ (Dick, 2019). The blue triangle represents endmember data from the fluid at Iced Bun and the green cross represents endmember data from Dog's Head.

Seewald and Seyfried, 1990; Seewald et al., 1994; Von Damm et al., 2005; Cruse and Seewald, 2006; Proskurowski et al., 2008; McDermott et al., 2018; Fiebig et al., 2019). Low concentrations of CH_4 at E2-S coupled to a relatively ^{13}C-enriched $\delta^{13}C_{CH4}$ isotopic composition of -7.0 and -7.6‰ rule out the influences of sediment thermogenesis and microbial derived CH_4 which would be expected to impart more ^{13}C-depleted signatures. Such ^{13}C-enriched $\delta^{13}C_{CH4}$ in combination with ^2H-enriched δD_{CH4} values (here: -98.7 and -99.9‰) have previously been associated to a 'potentially abiotic source' of origin (Kelley, 1996; Kelley and Früh-Green, 1999; Wang et al., 2018; McDermott et al., 2018; Klein et al., 2019). However, recent studies indicate that similar values can also be produced as a result of thermogenesis of seawater derived DOM – 'volcanic thermogenesis' (Fiebig et al., 2019; Reeves and Fiebig, 2020). As a result, the CH_4 abundances at E2-S could be a combination of volcanic thermogenesis with a possible contribution from an abiotic source.

An inverse relationship in CO_2 and CH_4 concentrations is observed in the fluids at E2-S such that high concentrations of CO_2 are matched with low CH_4 abundances. High CO_2 abundances are found in the most Cl-depleted fluid, while CH_4 concentrations are highest in the fluid containing with Cl concentrations. This

relationship could result from mixing of CH_4- and Cl-bearing hydrothermal fluids and a CO_2-enriched and Cl-poor magmatic vapour in the sub-surface of the E2-S vent site.

Magmatic Water Input

Stable oxygen and hydrogen isotopes in water in hydrothermal systems are mainly affected by three factors: i) interaction between the hydrothermal fluid and the host rock and/or sediments in the sub-surface, ii) phase separation and/or iii) contribution of mantle derived magmatic water. Hydration reactions between the hydrothermal fluids and the oceanic igneous crust yields increasing δD_{H2O} and $\delta^{18}O_{H2O}$ values with decreasing w/r ratios (**Supplementary Figure 4**, Bowers and Taylor, 1985; Bowers, 1989; Shanks et al., 1995; Shanks, 2001). The δD_{H2O} values in fluids from E2-S are depleted in ^2H relative to seawater (-2.0 to -1.2‰; **Supplementary Figure 4**). These low δD_{H2O} values are an indication that factors other than w/r interactions affect the H isotopic composition of these fluids.

Experimental work has shown that phase separation can affect the H and O isotope ratios of hydrothermal fluids (Horita et al., 1995; Berndt et al., 1996; Shmulovich et al., 1999; Foustoukos and Seyfried, 2007b). Vapours are slightly elevated in δD_{H2O} values

relative to the brine phase (Von Damm et al., 2003). Oxygen isotopes show the opposite fractionation direction: brines have higher $\delta^{18}O_{H2O}$ values than vapours (Berndt et al., 1996; Foustoukos and Seyfried, 2007b). The low chlorinity fluids analysed in this study show low δD_{H2O} and high $\delta^{18}O_{H2O}$ values (0.4 to 0.6‰), which is opposite of what would be expected for a vapour phase produced by phase separation. An influence of sediments on the fluid chemistry can also explain low δD_{H2O} combined with high $\delta^{18}O_{H2O}$ values (Baumberger et al., 2016; Toki et al., 2016). No sediment was observed at E2-S, and therefore sediment-fluid interactions are likely not responsible for the observed δD_{H2O} and $\delta^{18}O_{H2O}$ data.

The negative δD_{H2O} (-2.0 to -1.2‰) and positive $\delta^{18}O_{H2O}$ values (+0.4 to +0.6‰) in the E2-S hydrothermal vent fluids may indicate that a small fraction of the venting H_2O is derived from magmatic degassing. A constricted range of δD_{H2O} (-65.0 ± 20‰) and $\delta^{18}O_{H2O}$ (+6 ± 1‰, Taylor, 1979; Ohmoto, 1986) has been estimated to be of mantle derived magmatic water. Whereas water resulting from subduction related volcanic vapours (SRVV) have δD_{H2O} values ranging from -10 to -30‰ and $\delta^{18}O_{H2O}$ of +6 to +10‰ (Giggenbach, 1992; Hedenquist and Lowenstern, 1994). Fractionation related to degassing and slab-derived input of water can result in an increase in δD_{H2O} of magmatic waters at convergent margins (Taylor, 1986; Giggenbach, 1992; Hedenquist and Lowenstern, 1994; Taylor, 1997). Linear extrapolation of the fluids at E2-S indicate a possible small input of SRVV component into the fluids (**Figure 9**). Such an SRVV component input has been previously suggested to affect the PACMANUS hydrothermal vent fluids, Manus spreading centre, Papua New Guinea (Reeves et al., 2011), which show CO_2, $\delta^{13}C_{CO2}$, δD_{H2O} and $\delta^{18}O_{H2O}$ characteristics similar to those found at E2-S. The most plausible explanation for the δD_{H2O} and $\delta^{18}O_{H2O}$ data of the fluids venting at E2-S is that seawater-derived hydrothermal fluids underwent extensive water/rock interactions and mixing with small fractions of magmatic water vapour with a SRVV isotopic signature. Moreover, it appears that the fluid in 2010 did not have any involvement of an SRVV component as no highly negative δD_{H2O} values were reported (**Table 3A**). These variations seen at E2 in 2019 further provide a temporal evolution into the ESR systems.

Formation of Fluid at E2-W: Influence of Abiotic and Biotic Processes

The fluids diffusively venting at E2-W are low in temperature (53°C) relative to those emitted at E2-S (320°C, 344°C). Such diffuse low- to moderate-temperature fluids can be a result of either subseafloor mixing of high-temperature fluid with entrained seawater or they can represent conductively heated seawater (Cooper et al., 2000; McDermott et al., 2015b). The Mg depletion (42.6 mM) and K enrichment (13.4 mM) relative to seawater are a clear indication that the fluid at E2-W is a result of a high-temperature fluid that has undergone mixing with seawater prior to venting.
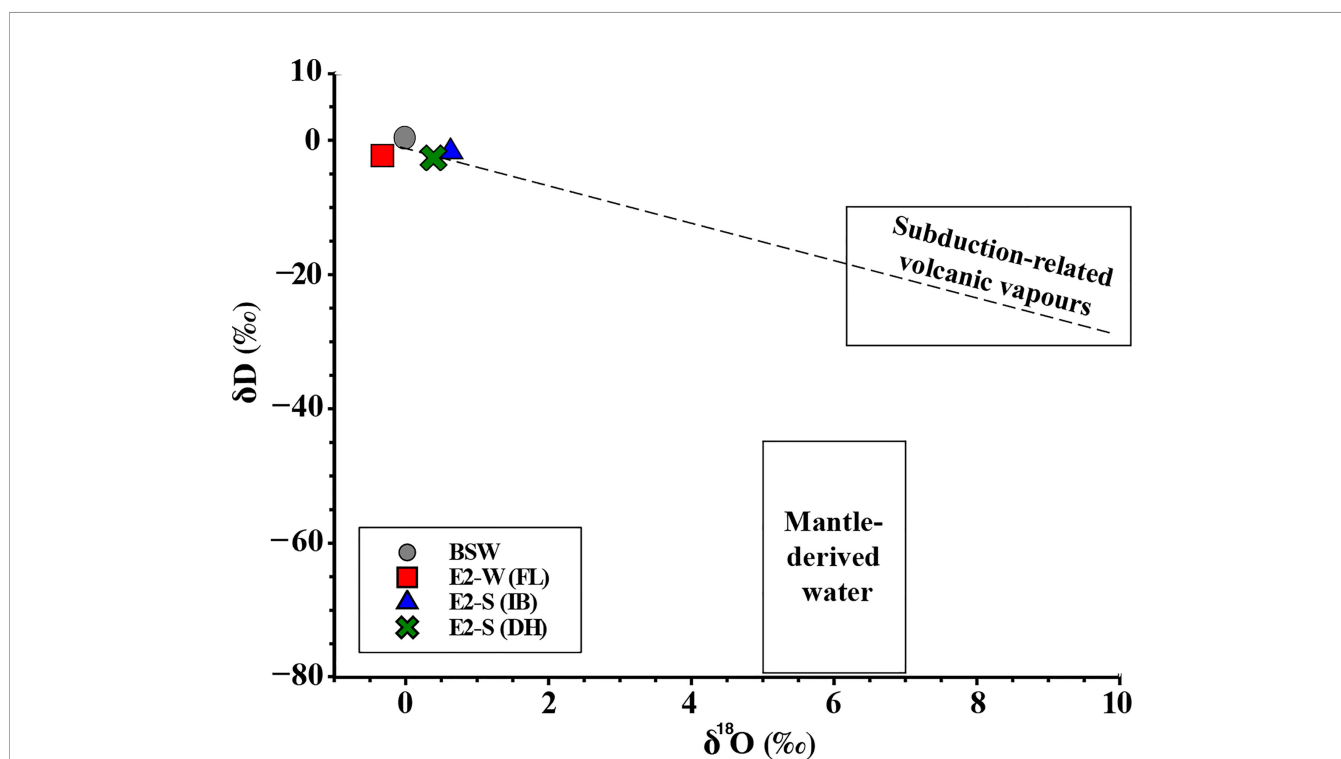
FIGURE 9 | Endmember water isotopic composition for E2-S and measured values for E2-W fluids. The dashed line is the least square regression line for the E2-S fluids and BSW. Data for subduction related volcanic vapours and mantle derived water were taken from Taylor, (1979; Ohmoto (1986) and Giggenbach (1992); Hedenquist and Lowenstern (1994), respectively.

The E2-W hydrothermal system is located about ca. 1.25 km north of the E2-S system. and the two vents investigated at E2-S, Dog's Head and Iced Bun, are fed by a single source fluid. E2-W is proximal enough to E2-S to be fed by fluids from the same root zone. To investigate the plausibility of the idea that a single deeply sourced fluid supplies all the E2 systems sampled in this study, an average composition of the endmember fluid (EF) for E2-S was computed and mixed with seawater (SW) until the Mg measured for the fluid at E2-W, was met (**Supplementary Table 2**). The Mg concentrations of the E2-W fluid reveal an EF: SW mixing ratio of 1:5. Enrichments and depletions of dissolved species in this hypothetical E2-W fluid (E2-W$_{calc}$) were then compared with the measured E2-W fluid (**Supplementary Table 2**). The excellent correspondence of calculated and measured data indicate that the E2-W fluid could indeed result from mixing of E2-S hydrothermal fluid with seawater. Na, Cl, Br, K, Ca and CO_2 values estimated are either within the analytical errors of the measurements (K, Ca and CO_2) or have seawater-like concentrations (Na, Cl and Br) indicating the fluid may derive from mixing between seawater and the common source fluid that feeds the E2-S vent sites.

Whereas most elements in the fluid at E2-W fit the conservative mixing model, enrichments (SO_4 and Sr) and depletions (H_2, CH_4, H_2S, Si and Fe) relative to the E2-W$_{calc}$ are observed. Si in hydrothermal systems is believed to behave conservatively and has been extensively used to constrain sub-surface conditions in these systems (Von Damm et al., 1991; Reeves et al., 2011; McDermott et al., 2018). However, depletions in Si relative to calculated E2-W$_{calc}$ observed is likely a result of sub-surface precipitation of silica. Janecky and Seyfried (1984) have shown that removal of silica through precipitation is only possible with the fluids that have undergone extensive cooling, which is also likely the case for the fluid at E2-W. Reaction path models further indicate this loss of Si in the modelled fluid because of quartz precipitation (**Supplementary Figure 5**).

The fluids at E2-W are enriched in SO_4 (by 2.27 mM) and Sr (by 1.98 µM) relative to the conservative mixing line. Sr in hydrothermal systems is known to substitute Ca in anhydrite precipitation (Kuhn et al., 2003). Therefore, the observed enrichments in Sr and SO_4 can be directly attributed to sub-seafloor dissolution of anhydrite. Endmember extrapolation of SO_4 at E2-W reveals a concentration of 13 mM. These strong SO_4 excesses have commonly been interpreted as evidence of anhydrite dissolution (e.g., Reeves et al., 2011).

Aerobic sulphide oxidation (equation 1) is another possible source of excess sulphate. Indeed, thermodynamic computations indicate that the major source of catabolic energy in the E2-W subseafloor is aerobic sulphide oxidation (**Figure 10**). Furthermore, non-sedimented hydrothermal systems are known to host a variety of sulphide oxidizing microorganisms (Dahle et al., 2015; Dahle et al., 2018). Microbial sulphide oxidation could also further help explain the depletion of H_2S in the fluid (<0.2 µM, below limit of quantification) compared to the calculated 0.81 mM abundance that would be expected if conservative mixing were occurring. However, even if 0.8 mM of H_2S were oxidized to sulphate, the sulphate enrichments of 2.27 mM cannot be fully

explained by this process. Moreover, abiotic precipitation of pyrite is another possible sink for H_2S. Indeed, depletion of H_2S is matched by a loss of >90% of the dissolved Fe, which could point to pyrite precipitation. While Fe is likely only affected by abiotic reactions, SO_4 and H_2S concentrations at E2-W could be a result of both biotic as well as abiotic reactions taking place in the sub-surface. We suggest that most of the sulphate excess is due to anhydrite dissolution, whereas H_2S is lost as consequence of pyrite precipitation as well as aerobic sulphide oxidation.

A strong depletion of H_2 relative to the conservative mixing line is also observed in the fluids at E2-W (**Supplementary Table 2**). H_2 in mixing zones in hydrothermal systems can be consumed by the reduction of CO_2 to formic species (McDermott et al., 2015b). If CH_4 was a metabolic product of CO_2 reduction, CH_4 concentrations in the fluids should be higher than predicted from conservative mixing. This is not the case, as the fluid at E2-W is depleted in CH_4 relative to the mixing line by 5.27 µM (**Supplementary Table 2**). Such a depletion of CH_4 at E2-W is likely the result of aerobic oxidation of CH_4 (**Figure 10**). CO_2 and H_2 concentrations of the fluids are inconclusive in this regard, as a H_2 consumption of 8 µM would deplete CO_2 only by 2 µM, which is small relative to the 300 µM mismatch between measured and calculated composition (**Supplementary Table 2**). Moreover, CO_2 could be produced by oxidation of CH_4 by microorganisms. $\delta^{13}C_{CO2}$ at E2-W is -10.8‰ and is more ^{13}C-depleted than the measured $\delta^{13}CO_2$ values at E2-S of -3.7‰ and -4.4‰. If the CO_2 at E2-S is a result of magmatic degassing and the entire E2 system is fed by a common root zone, then a range of $\delta_{13}C_{CO2}$ between -4.4‰ to 0.3‰ would be predicted at E2-W if it simply reflects mixing between the E2-S endmember and seawater. The far more ^{13}C-depleted values of $\delta^{13}C_{CO2}$ at E2-W suggest an additional, non-magmatic source of CO_2 in the vent fluids. Such more negative values of $\delta^{13}C_{CO2}$ relative to the high-temperature fluid have been previously observed at EPR and have been attributed to methanotrophy (Proskurowski et al., 2008). The idea that methane oxidation may contribute to the dissolved CO_2 pool is further supported by catabolic landscape models, which indicate that this aerobic methane oxidation is indeed exergonic at E2-W (**Figure 10**). It is likely that the $\delta^{13}C_{CO2}$ at E2-W represents a combination of the endmember fluid mixed with seawater with contributions from microbial metabolism.

Implications for Surface and Sub-Surface Ecology at E2

A more general assessment of the catabolic energy landscape at E2 is warranted as endmember fluids at E2-S are enriched in H_2S, CH_4, CO_2, H_2, Fe and Mn relative to seawater. The enrichments of these components are a result of high-temperature fluid-rock interaction and magmatic degassing taking place in the sub-surface. A combination of these processes creates an energy gradient representing an appropriate environment for life in the deep-sea at E2 to thrive on.

Just like we established for the E2-W site, this reduced fluid can mix with the oxic seawater entrained in the subseafloor and create an energy rich environment for catabolic reactions to take place (**Figure 10A**, McCollom and Shock, 1997; Amend et al., 2011).
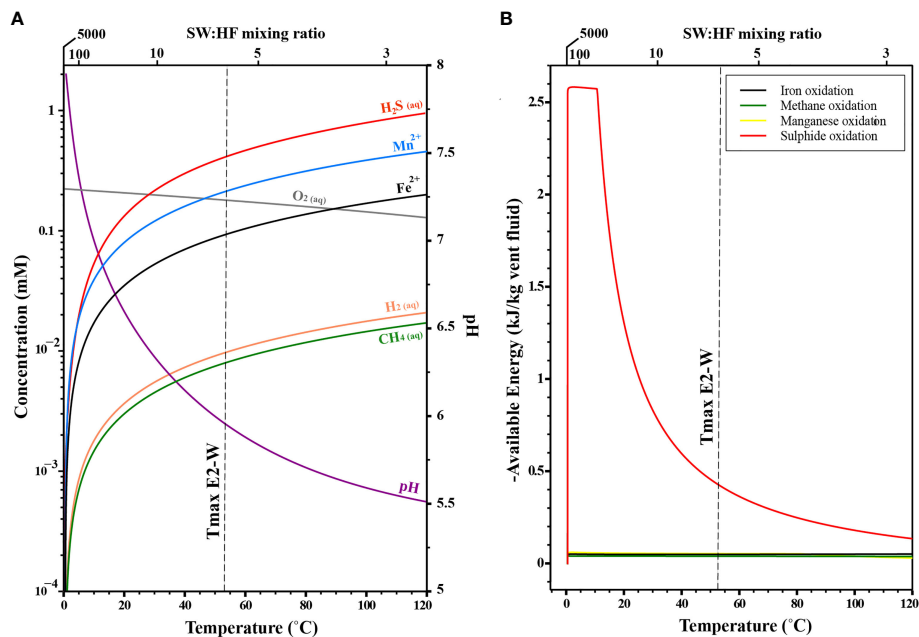
FIGURE 10 | Thermodynamic models for chemical gradient and associated energy landscape at E2. **(A)** Modelled concentration of various species as a function of temperature and mixing ratios. **(B)** Modelled energy available for the various reactions as a function of temperature and mixing ratios.

These reactions (**Table 2**) help support a chemosynthetic ecosystem at E2. The catabolic energy computations we conducted indicate that aerobic sulphide oxidation (ASO) is clearly the dominant energy source at both low and high temperatures (**Figure 10B**). Between 120 and 60°C (i.e., at low SW: HF mixing ratios) ASO has an energy yield between -0.2 and -0.4 kJ/kg of vent fluid. At temperatures <60°C (i.e., high SW: HF mixing ratios), the models predict a higher energy yield as high as -2.6 kJ/kg of vent fluid.

Aerobic methane oxidation (AMO) is the next most abundant energy source predicted at E2 (**Figure 10B**). At high temperatures (120 to 60°C), AMeO has an energy yield of ∼ -0.03 kJ/kg of vent fluid, and the energy yield may approach -0.8 kJ/kg for vent fluid at lower temperature. Aerobic iron oxidation (AFeO) and aerobic manganese oxidation (AMnO) account for the lowest energy availability at E2.

The modelling results presented are valid for conservative mixing of hydrothermal fluids with seawater. Conductive cooling, mixing with entrained seawater and related abiotic processes at E2 can greatly affect the composition of the hydrothermal fluids. Studies have shown that abiotic reactions can indeed reduce the energy available for catabolic reactions (McDermott et al., 2020).

The effect of mixing on the energy availability is evident at E2-W, where the fluids have been extensively mixed with BSW prior to venting and have a SW: HF mixing ratio of 5:1. Although the H_2S in the fluid was below <0.8 mM, large microbial mats were observed that covered the flange. In contrast, such features were not evident in the E2-S system. Thermodynamic models predict that these H_2S-depleted and O_2-enriched fluid-seawater mixtures coincide with peak energy availabty to chemosynthetic microbial communities (**Figures 10A, B**).

ASO and AMO are the dominant energy source for all the E2 vents. Large areas of the E2-S have been known to be inhabited by biota that are dependent on mainly ASO for their metabolic pathways (Rogers et al., 2012). The temperature range, extensive mixing with BSW, fluid chemistry and predicted thermodynamic modelling indicate that the conditions at E2-W are suitable to host a robust sub-surface biosphere.

SUMMARY

The chemical and isotopic compositions of hydrothermal fluids from the E2 segment of the ESR are useful guides to subseafloor processes of phase separation, water-rock reactions, and mixing with entrained seawater, followed by pyrite precipitation. Depletion in Cl in the high-temperature fluid at E2-S is attributed to phase separation. Low Fe/Mn ratios and pyrite precipitation indicate that the fluids have undergone excessive conductive cooling in the sub-seafloor prior to venting. The H_2 concentration in the fluids at E2-S are likely a result of equilibration with the hematite-magnetite buffer. The H_2S concentrations in the fluid represents mantle derived sulphur contribution that varies from 81 and 69% relative to seawater derived sulphur of about 19 and 31% in these fluids. CH_4 formation in the fluid can be either from a volcanic thermogenesis of seawater-sourced DOM and/or leaching of abiotic CH_4 from fluid inclusions. The high CO_2 abundances and $\delta^{13}C_{CO2}$ and δD_{H2O} values are evidence that the fluid at E2-S is affected by magmatic components.

The lower temperatures and higher water-rock ratios, along with lower REE, higher Na/Cl and lower Ca/Cl, Li/Cl and Cs/Cl ratios in this study compared to the fluids sampled in 2010

indicate that the root zone has undergone changes towards a slightly more altered basement over the past 9 years. The enriched dissolved gases present in the circulating fluid are a result of combination of fluid-rock interactions and magmatic degassing taking place in the sub-surface. Our data hence indicates progressive alteration of basement in the root zone along with evidence for magmatic degassing taking place at E2. Moreover, mixing of magmatic vapour and elevated $\delta^{13}C_{CO2}$ could reflect replenishing of the magma chamber at E2.

The mixed fluid at E2-W and E2-S appear to originate from a single source fluid at depth (>300 bar). The fluid at E2-W shows enrichments in Sr and SO_4 that can be attributed to anhydrite dissolution. However, aerobic sulphide oxidation could be an additional source for SO_4 and a sink for H_2S. Depletion of H_2S and Fe observed in the fluid at E2-W is a result of pyrite precipitation taking place in the sub-surface. Depleted Si relative to the conservative mixing models reflect loss of Si due to precipitation of amorphous silica. CH_4 depletions in the fluid are likely a result of aerobic methane oxidation. H_2 depletions in the fluid can be either a result of microbial respiration in the sub-seafloor (aerobic hydrogen oxidation) or by reactions involving O_2 and NO_3^- in the mixing zones. Geochemical reaction path models for E2 indicate that mixing of hydrothermal fluids with entrained seawater can support subseafloor microbial life, with aerobic oxidation of sulphide and methane being potent catabolic energy sources.

Our study provides novel insights into the temporal evolution of the E2-S hydrothermal system that may expand our understanding of hydrothermal systems hosted in BABs. Bioenergetics calculations indicate that H_2S is the main provider of catabolic energy followed by CH_4, Fe and H_2. Our findings at E2-W further suggest that these energy sources may indeed be utilized by subseafloor microbial communities.

DATA AVAILABILITY STATEMENT

The original contributions presented in the study are included in the article/**Supplementary Material**. Further inquiries can be directed to the corresponding author.

REFERENCES

Amend, J. P., McCollom, T. M., Hentscher, M., and Bach, W. (2011). Catabolic and Anabolic Energy for Chemolithoautotrophs in Deep-Sea Hydrothermal Systems Hosted in Different Rock Types. *Geochim. Cosmochim. Acta* 75 (19), 5736–5748. doi: 10.1016/j.gca.2011.07.041

Atkinson, A. B. Jr (2002). A Model for the PTX Properties of H_2O-NaCl (Doctoral dissertation, Virginia Tech). *MSc. Thesis. Virgin. Tech*, 133pp

Baker, T., and Lang, J. R. (2001). Fluid Inclusion Characteristics of Intrusion-Related Gold Mineralization, Tombstone-Tungsten Magmatic Belt, Yukon Territory, Canada. *Mineral. Deposit.* 36 (6), 563–582. doi: 10.1007/s001260100189

Baumberger, T., Früh-Green, G. L., Thorseth, I. H., Lilley, M. D., Hamelin, C., Bernasconi, S. M., et al. (2016). Fluid Composition of the Sediment-Influenced Loki's Castle Vent Field at the Ultra-Slow Spreading Arctic Mid-Ocean Ridge. *Geochim. Cosmochim. Acta* 187, 156–178. doi: 10.1016/j.gca.2016.05.017

AUTHOR CONTRIBUTIONS

FUNDING

ACKNOWLEDGMENTS

SUPPLEMENTARY MATERIAL

The Supplementary Material for this article can be found online at: https://www.frontiersin.org/articles/10.3389/fmars.2022.765648/full#supplementary-material

Beermann, O., Garbe-Schönberg, D., Bach, W., and Holzheid, A. (2017). Time-Resolved Interaction of Seawater With Gabbro: An Experimental Study of Rare-Earth Element Behavior Up to 475 °C, 100 Mpa. *Geochim. Cosmochim. Acta* 197, 167–192. doi: 10.1016/j.gca.2016.10.016

Berndt, M. E., Seal, R. R., Shanks, W. C., and Seyfried, W. E. (1996). Hydrogen Isotope Systematics of Phase Separation in Submarine Hydrothermal Systems: Experimental Calibration and Theoretical Models. *Geochim. Cosmochim. Acta* 60 (9), 1595–1604. doi: 10.1016/0016-7037(96)00033-6

Berndt, M. E., and Seyfried, W. E. (1990). Boron, Bromine, and Other Trace Elements as Clues to the Fate of Chlorine in Mid-Ocean Ridge Vent Fluids. *Geochim. Cosmochim. Acta* 54 (8), 2235–2245. doi: 10.1016/0016-7037(90)90048-P

Berndt, M. E., and Seyfried, W. E. (1993). Calcium and Sodium Exchange During Hydrothermal Alteration of Calcic Plagioclase at 400°C and 400 Bars. *Geochim. Cosmochim. Acta* 57 (18), 4445–4451. doi: 10.1016/0016-7037(93)90494-H

Berndt, M. E., Seyfried, W. E., and Janecky, D. R. (1989). Plagioclase and Epidote Buffering of Cation Ratios in Mid-Ocean Ridge Hydrothermal Fluids:

Experimental Results in and Near the Supercritical Region. *Geochim. Cosmochim. Acta* 53 (9), 2283–2300. doi: 10.1016/0016-7037(89)90351-7

Bieseler, B., Diehl, A., Jöns, N., Lucassen, F., and Bach, W. (2018). Constraints on Cooling of the Lower Ocean Crust From Epidote Veins in the Wadi Gideah Section, Oman Ophiolite. *Geochem. Geophys. Geosyst.* 19 (11), 4195–4217. doi: 10.1029/2018GC007679

Bischoff, J. L. (1991). Densities of Liquids and Vapors in Boiling NaCl-H$_2$O Solutions: A Pvtx Summary From 300° to 500°C. *Am. J. Sci.* 291(4), pp.309–338. doi: 10.2475/ajs.291.4.309

Bischoff, J. L., and Pitzer, K. S. (1989). Liquid-Vapor Relations for the System NaCl-H$_2$O: Summary of the P-T- X Surface From 300° to 500°C. *Am. J. Sci.* 289 (3), pp.217–248. doi: 10.2475/ajs.289.3.217

Bischoff, J. L., and Rosenbauer, R. J. (1985). An Empirical Equation of State for Hydrothermal Seawater (3.2 Percent Nacl). *Am. J. Sci.* 285 (8), 725–763. doi: 10.2475/ajs.285.8.725

Bodnar, R. J., Samson, I., Anderson, A., and Marshall, D. (2003). Reequilibration of Fluid Inclusions." Fluid Inclusions: Analysis and Interpretation. 32, 213–230

Bohrmann, G. (2019). The Expedition PS119 of the Research Vessel POLARSTERN to the Eastern Scotia in 2019. *Reports on Polar and Marine Research*, Alfred-Wegener-Institut, Helmholtz-Zentrum für Polar- und Meeresforschung, Bremerhaven, Germany, 736. doi: 10.2312/BzPM_0736_2019

Bowers, T. S. (1989). Stable Isotope Signatures of Water-Rock Interaction in Mid-Ocean Ridge Hydrothermal Systems: Sulfur, Oxygen, and Hydrogen. *J. Geophys. Res.* 94 (B5), 5775–5786. doi: 10.1029/JB094iB05p05775

Bowers, T. S., and Taylor, H. P. (1985). An Integrated Chemical and Stable-Isotope Model of the Origin of Midocean Ridge Hot Spring Systems. *J. Geophys. Res: Solid Earth* 90(B14),pp.12583–12606. doi: 10.1029/jb090ib14p12583

Bruguier, N. J., and Livermore, R. A. (2001). Enhanced Magma Supply at the Southern East Scotia Ridge: Evidence for Mantle Flow Around the Subducting Slab? *Earth Planet. Sci. Lett.* 191 (1–2), 129–144. doi: 10.1016/S0012-821X(01)00408-3

Butterfield, D. A., Nakamura, K. I., Takano, B., Lilley, M. D., Lupton, J. E., Resing, J. A., et al. (2011). High SO$_2$ Flux, Sulfur Accumulation, and Gas Fractionation at an Erupting Submarine Volcano. *Geology* 39 (9), 803–806. doi: 10.1130/G31901.1

Cline, J. D. (1969). Spectrophotometric Determination of Hydrogen Sulfide in Natural Waters. *Limnol. Oceanog.* 14 (3), 454–458. doi: 10.4319/lo.1969.14.3.0454

Cole, C. S., James, R. H., Connelly, D. P., and Hathorne, E. C. (2014). Rare Earth Elements as Indicators of Hydrothermal Processes Within the East Scotia Subduction Zone System. *Geochim. Cosmochim. Acta* 140, 20–38. doi: 10.1016/j.gca.2014.05.018

Cooper, M. J., Elderfield, H., and Schultz, A. (2000). Diffuse Hydrothermal Fluids From Lucky Strike Hydrothermal Vent Field: Evidence for a Shallow Conductively Heated System. *J. Geophys. Res.: Solid. Earth* 105 (B8), 19369–19375. doi: 10.1029/2000jb900138

Craddock, P. R., Bach, W., Seewald, J. S., Rouxel, O. J., Reeves, E., and Tivey, M. K. (2010). Rare Earth Element Abundances in Hydrothermal Fluids From the Manus Basin, Papua New Guinea: Indicators of Sub-Seafloor Hydrothermal Processes in Back-Arc Basins. *Geochim. Cosmochim. Acta* 74 (19), 5494–5513. doi: 10.1016/j.gca.2010.07.003

Craig, H. (1970). Abyssal Carbon 13 in the South Pacific. *J. Geophys. Res.* 75 (3), 691–695. doi: 10.1029/jc075i003p00691

Cruse, A. M., and Seewald, J. S. (2006). Geochemistry of Low-Molecular Weight Hydrocarbons in Hydrothermal Fluids From Middle Valley, Northern Juan De Fuca Ridge. *Geochim. Cosmochim. Acta* 70 (8), 2073–2092. doi: 10.1016/j.gca.2006.01.015

Dahle, H., Økland, I, Thorseth, I. H., Pederesen, R. B., and Steen, I. H. (2015). Energy Landscapes Shape Microbial Communities in Hydrothermal Systems on the Arctic Mid-Ocean Ridge. *ISME. J.* 9 (7), 1593–1606. doi: 10.1038/ismej.2014.247

Dahle, H., Le Moine Bauer, S, Baumberger, T., Stokke, R., Pedersen, R. B., Thorseth, I. H., et al. (2018). Energy Landscapes in Hydrothermal Chimneys Shape Distributions of Primary Producers. *Front. Microbiol.* 9. doi: 10.3389/fmicb.2018.01570

De Ronde, C. E., and Jambor, J. L. (1995). Fluid Chemistry and Isotopic Characteristics of Seafloor Hydrothermal Systems and Associated Vms Deposits: Potential for Magmatic Contributions. *Magma. Fluid. Ore. Deposit.* 23 (1), 479–509.

Dick, J. M. (2019). Chnosz: Thermodynamic Calculations and Diagrams for Geochemistry. *Front. Earth Sci.* 7, 150. doi: 10.3389/feart.2019.00180

Diehl, A., and Bach, W. (2020b). MARHYS (Marine HYdrothermal Solutions) Database: A Global Compilation of Marine Hydrothermal Vent Fluid, End Member and Seawater Compositions. *Geochem. Geophys. Geosyst.* 21(12), p.e2020GC009385. doi: 10.1029/2020GC009385

Diehl, A., and Bach, W. (2021). *Marhys Database 2.0. Pangaea.* doi 10.1594/PANGAEA.935649.

Diehl, A., De Ronde, C. E. J., and Bach, W. (2020a). Subcritical phase separation and occurrence of deep-seated brines at the NW Caldera vent field, Brothers volcano: evidence from fluid inclusions in Hydrothermal Precipitates. *Geofluids.* doi: 10.1155/2020/8868259

Douville, E., Bienvenu, P., Charlou, J. P., Donval, J. P., Fouquet, Y., Appriou, P., et al. (1999). Yttrium and Rare Earth Elements in Fluids From Various Deep-Sea Hydrothermal Systems - Evidence for Heat Extraction From Magma Chambers or Cracking Fronts? *Geochim. Cosmochim. Acta* 63 (5), 627–643. doi: 10.1016/S0016-7037(99)00024-1

Douville, E., Charlou, J. L., Oelkers, E. H., Bienvenu, P., Jove Colon, C. F., Donval, J. P., et al. (2002). The Rainbow Vent Fluids (36°14′N, MAR): The Influence of Ultramafic Rocks and Phase Separation on Trace Metal Content in Mid-Atlantic Ridge Hydrothermal Fluids. *Chem. Geolog.* 184 (1–2), 37–48. doi: 10.1016/S0009-2541(01)00351-5

Driesner, T. (2007). The System H$_2$O-NaCl. Part II: Correlations for Molar Volume, Enthalpy, and Isobaric Heat Capacity From 0 to 1000°C, 1 to 5000 Bar, and 0 to 1 Xnacl. *Geochim. Cosmochim. Acta* 71 (20), 4902–4919. doi: 10.1016/j.gca.2007.05.026

Driesner, T., and Heinrich, C. A. (2007). The System H$_2$O-NaCl. Part I: Correlation Formulae for Phase Relations in Temperature-Pressure-Composition Space From 0 to 1000 °C, 0 to 5000 Bar, and 0 to 1 XNaCl. *Geochim. Cosmochim. Acta* 71 (20), 4880–4901. doi: 10.1016/j.gca.2006.01.033

Evans, W. C., White, L. D., and Rapp, J. B. (1988). Geochemistry of Some Gases in Hydrothermal Fluids From the Southern Juan De Fuca Ridge. *J. Geophys. Res* 93(B12), pp.15305–15313. doi: 10.1029/jb093ib12p15305

Fiebig, J., Stefánsson, A., Ricci, A., Tassi, F., Viveiros, F., Silva, C., et al. (2019). Abiogenesis Not Required to Explain the Origin of Volcanic-Hydrothermal Hydrocarbons. *Geochem. Perspect. Lett.* 11, 23–27. doi: 10.7185/geochemlet.1920

Foustoukos, D. I., and Seyfried, W. E. (2007a). Trace Element Partitioning Between Vapor, Brine and Halite Under Extreme Phase Separation Conditions. *Geochim. Cosmochim. Acta* 71 (8), 2056–2071. doi: 10.1016/j.gca.2007.01.024

Foustoukos, D. I., and Seyfried, W. E. (2007b). Fluid Phase Separation Processes in Submarine Hydrothermal Systems. *Rev. Mineral. Geochem.* 65, 213–239. doi: 10.2138/rmg.2007.65.7

Foustoukos, D. I., and Seyfried, W. E. (2007c). Quartz Solubility in the Two-Phase and Critical Region of the NaCl-KCl-H$_2$O System: Implications for Submarine Hydrothermal Vent Systems at 9°50′N East Pacific Rise. *Geochim. Cosmochim. Acta* 71 (1), 186–201. doi: 10.1016/j.gca.2006.08.038

Fretzdorff, S., Livermore, R. A., Devey, C. W., Leat, P. T., and Stoffers, P. (2002). Petrogenesis of the Back-Arc East Scotia Ridge, South Atlantic Ocean. *J. Petrolog.* 43 (8), 1435–1467. doi: 10.1093/petrology/43.8.1435

Gallant, R. M., and Von Damm, K. L. (2006). Geochemical Controls on Hydrothermal Fluids From the Kairei and Edmond Vent Fields, 23°-25°S, Central Indian Ridge. *Geochem. Geophys. Geosyst.* 7 (6), 1–24. doi: 10.1029/2005GC001067

German, C. R., Livermore, R. A., Baker, E. T., Bruguier, N. I., Connelly, D. P., Cunningham, A. P., et al. (2000). Hydrothermal Activity on the East Scotia Ridge: An Isolated High-Latitude Back-Ark Spreading Centre. *Earth Planet. Sci. Lett.*, 184(1) 241–250. doi: 10.1016/S0012-821X(00)00319-8

Giggenbach, W. F. (1992). Isotopic Shifts in Waters From Geothermal and Volcanic Systems Along Convergent Plate Boundaries and Their Origin. *Earth Planet. Sci. Lett.* 113 (4), 495–510. doi: 10.1016/0012-821X(92)90127-H

Haar, L. (1984). NBS/NRC Steam Tables. CRC Press

Haar, V. L., Gallagher, J. S., and Kell, G. S. (1985). NBS/NRC Steam Tables. *Chem. Ing. Tech.* 57, 812–812. doi: 10.1002/cite.330570931

Hedenquist, J. W., and Lowenstern, J. B. (1994). The Role of Magmas in the Formation of Hydrothermal Ore Deposits. *Nature* 370 (August), 519–527. doi: 10.1038/370519a0

Herrera, S., Watanabe, H., and Shank, T. M. (2015). Evolutionary and Biogeographical Patterns of Barnacles From Deep-Sea Hydrothermal Vents. *Mol. Ecol.* 24 (3), 673–689. doi: 10.1111/mec.13054

Holloway, J. R., and Blank, J. G. (1994). "Application of Experimental Results to C-O-H Species in Natural Melts," in *Rev. Mineral Geochem.* 30 (1), 187–230

Horita, J., Cole, D. R., and Wesolowski, D. J. (1995). The Activity-Composition Relationship of Oxygen and Hydrogen Isotopes in Aqueous Salt Solutions: Iii. Vapor-Liquid Water Equilibration of NaCl Solutions to 350°C. *Geochim. Cosmochim. Acta* 59 (6), 1139–1151. doi: 10.1016/0016-7037(95)00031-T

Ishibashi, J., and Urabe, T. (1995). Hydrothermal Activity Related to Arc-Backarc Magmatism in the Western Pacific. In: Backarc Basins. Boston, MA: Springer, 451–495. doi: 10.1007/978-1-4615-1843-3_13

James, R. H., Green, D. R. H., Stock, M. J., Alker, B. J., Banerjee, N. R., Cole, C., et al. (2014). Composition of Hydrothermal Fluids and Mineralogy of Associated Chimney Material on the East Scotia Ridge Back-Arc Spreading Centre. *Geochim. Cosmochim. Acta* 139, 47–71. doi: 10.1016/j.gca.2014.04.024

Janecky, D. R., and Seyfried, W. E. (1984). Formation of Massive Sulfide Deposits on Oceanic Ridge Crests: Incremental Reaction Models for Mixing Between Hydrothermal Solutions and Seawater. *Geochim. Cosmochim. Acta* 48 (12), 2723–2738. doi: 10.1016/0016-7037(84)90319-3

Javoy, M., Pineau, F., and Iiyama, I. (1978). Experimental Determination of the Isotopic Fractionation Between Gaseous CO_2 and Carbon Dissolved in Tholeiitic Magma. *Contrib. Mineral. Petrol.* 67 (1), 35–39. doi: 10.1007/BF00371631

Johnson, J. W., Oelkers, E. H., and Helgeson, H. C. (1992). Supcrt92: A Software Package for Calculating the Standard Molal Thermodynamic Properties of Minerals, Gases, Aqueous Species, and Reactions From 1 to 5000 Bar and 0 to 1000°C. *Comput. Geosci.* Vol. 18 (7), pp.899–947. doi: 10.1016/0098-3004(92)90029-Q

Kelley, D. S. (1996). Methane-Rich Fluids in the Oceanic Crust. *J. Geophys. Res. B.: Solid. Earth* 101 (2), 2943–2962. doi: 10.1029/95JB02252

Kelley, D. S., and Früh-Green, G. L. (1999). Abiogenic Methane in Deep-Seated Mid-Ocean Ridge Environments: Insights From Stable Isotope Analyses. *J. Geophys. Res.: Solid. Earth* 104 (B5), 10439–10460. doi: 10.1029/1999jb900058

Klein, F., Grozeva, N. G., and Seewald, J. S. (2019). Abiotic Methane Synthesis and Serpentinization in Olivine-Hosted Fluid Inclusions. *Proc. Natl. Acad. Sci. Unite. States America* 116 (36), 17666–17672. doi: 10.1073/pnas.1907871116

Kuhn, T., Herzig, P. M., Hannington, M. D., Garbe-Schönberg, D., and Stoffers, P. (2003). Origin of Fluids and Anhydrite Precipitation in the Sediment-Hosted Grimsey Hydrothermal Field North of Iceland. *Chem. Geolog.* 202 (1–2), 5–21. doi: 10.1016/S0009-2541(03)00207-9

Larter, R. D., Vanneste, L. E., Morris, P., and Smythe, D. K. (2003). Structure and Tectonic Evolution of the South Sandwich Arc. *Geolog. Soc. Special. Publ.* 219 (1), 255–284. doi: 10.1144/GSL.SP.2003.219.01.13

Leat, P. T., Fretwell, P. T., Tate, A. J., Larter, R. D., Martin, T. J., Smellie, J. L, et al (2016). Bathymetry and Geological Setting of the South Sandwich Islands Volcanic Arc.. *Antarct. Sci* 28 (4), 293–303

Leat, P. T., Livermore, R. A., Millar, I. L., and Pearce, J. A. (2000). Magma Supply in Back-Arc Spreading. *J. Petrolog.* 41 (6), 845–866. doi: 10.1093/petrology/41.6.845

Leat, P. T., Pearce, J. A., Barker, P. F., Millar, I. L., Barry, T. L., and Larter, R. D. (2004). Magma Genesis and Mantle Flow at a Subducting Slab Edge : The South Sandwich Arc-Basin System. *Earth Planet. Sci. Lett.* 227, 17–35. doi: 10.1016/j.epsl.2004.08.016

Linse, K., Copley, J. T., Connelly, D. P., Larter, R. D., Pearce, D. A., Polunin, N. V. C., et al. (2019). Fauna of the Kemp Caldera and Its Upper Bathyal Hydrothermal Vents (South Sandwich Arc, Antarctica). *R. Soc. Open Sci.* 6, (11). doi: 10.1098/rsos.191501

Livermore, R., Cunningham, A., Vanneste, L., and Larter, R. (1997). Subduction Influence on Magma Supply at the East Scotia Ridge. *Earth Planet. Sci. Lett.* 150 (3–4), 261–275. doi: 10.1016/s0012-821x(97)00074-5

Lupton, J., Butterfield, D., Lilley, M., Evans, L., Nakamura, K. I., Chadwick, W., et al. (2006). Submarine Venting of Liquid Carbon Dioxide on a Mariana Arc Volcano. *Geochem. Geophys. Geosyst.* 7, (8). doi: 10.1029/2005GC001152

Mattey, D. P. (1991). Carbon Dioxide Solubility and Carbon Isotope Fractionation in Basaltic Melt. *Geochim. Cosmochim. Acta* 55 (11), 3467–3473. doi: 10.1016/0016-7037(91)90508-3

Mattey, D. P., Carr, R. H., Wright, I. P., and Pillinger, C. T. (1984). Carbon Isotopes in Submarine Basalts. *Earth Planet. Sci. Lett.* 70 (2), 196–206. doi: 10.1016/0012-821X(84)90005-0

McCollom, T. M. (2007). Geochemical Constraints on Sources of Metabolic Energy for Chemolithoautotrophy in Ultramafic-Hosted Deep-Sea Hydrothermal Systems. *Astrobiology* 7 (6), 933–950. doi: 10.1089/ast.2006.0119

McCollom, T. M., and Shock, E. L. (1997). Geochemical Constraints on Chemolithoautotrophic Metabolism by Microorganisms in Seafloor Hydrothermal Systems. *Geochim. Cosmochim. Acta* 61 (20), 4375–4391. doi: 10.1016/S0016-7037(97)00241-X

McDermott, J. M., Ono, S., Tivey, M. K., Seewald, J. S., Shanks, W. C., and Solow, A. R. (2015a). Identification of Sulfur Sources and Isotopic Equilibria in Submarine Hot-Springs Using Multiple Sulfur Isotopes. *Geochim. Cosmochim. Acta* 160, 169–187. doi: 10.1016/j.gca.2015.02.016

McDermott, J. M., Seewald, J. S., German, C. R., and Sylva, S. P. (2015b). Pathways for Abiotic Organic Synthesis at Submarine Hydrothermal Fields. *Proc. Natl. Acad. Sci. Unite. States America* 112 (25), 7668–7672. doi: 10.1073/pnas.1506295112

McDermott, J. M., Sylva, S. P., Ono, S., German, C. R., and Seewald, J. S. (2018). Geochemistry of Fluids From Earth's Deepest Ridge-Crest Hot-Springs: Piccard Hydrothermal Field, Mid-Cayman Rise. *Geochim. Cosmochim. Acta* 228, 95–118. doi: 10.1016/j.gca.2018.01.021

McDermott, J. M., Sylva, S. P., Ono, S., German, C. R., and Seewald, J. S. (2020). Abiotic Redox Reactions in Hydrothermal Mixing Zones: Decreased Energy Availability for the Subsurface Biosphere. *Proc. Natl. Acad. Sci.*, 117 (34), 20453–20461. doi: 10.1073/pnas.2003108117

Merlivat, L., Pineau, F., and Javoy, M. (1987). Hydrothermal Vent Waters at 13°N on the East Pacific Rise: Isotopic Composition and Gas Concentration. *Earth Planet. Sci. Lett.* 84 (1), 100–108. doi: 10.1016/0012-821X(87)90180-4

Mottl, M. J., and Holland, H. D. (1978). Chemical Exchange During Hydrothermal Alteration of Basalt by Seawater-I. Experimental Results for Major and Minor Components of Seawater. *Geochim. Cosmochim. Acta* 42 (8), 1103–1115. doi: 10.1016/0016-7037(78)90107-2

Mottl, M. J., Seewald, J. S., Wheat, C. G., Tivey, M. K., Michael, P. J., Proskurowski, G., et al. (2011). Chemistry of Hot Springs Along the Eastern Lau Spreading Center. *Geochim. Cosmochim. Acta* 75 (4), 1013–1038. doi: 10.1016/j.gca.2010.12.008

Ohmoto, H. (1986). "Stable Isotope Geochemistry of Ore Deposits." in Stable Isotopes in High Temperature Geological Processes De Gruyter. 491–560. doi: 10.1515/9781501508936-019

Pape, T., Bünz, S., Hong, W. L., Torres, M. E., Riedel, M., Panieri, G., et al. (2020a). Origin and Transformation of Light Hydrocarbons Ascending at an Active Pockmark on Vestnesa Ridge, Arctic Ocean. *J. Geophys. Res.: Solid. Earth* 125, (1). doi: 10.1029/2018JB016679

Pape, T., Haeckel, M., Riedel, M., Kölling, M., Schmidt, M., Wallmann, K., et al. (2020b). Formation Pathways of Light Hydrocarbons in Deep Sediments of the Danube Deep-Sea Fan, Western Black Sea. *Mar. Petrol. Geolog.* 122, 104627. doi: 10.1016/j.marpetgeo.2020.104627

Pester, N. J., Reeves, E. P., Rough, M. E., Ding, K., Seewald, J. S., and Seyfried, W. E. (2012). Subseafloor Phase Equilibria in High-Temperature Hydrothermal Fluids of the Lucky Strike Seamount (Mid-Atlantic Ridge, 37°17'n). *Geochim. Cosmochim. Acta* 90, 303–322. doi: 10.1016/j.gca.2012.05.018

Peter, J.M., and Scott, S. D. (1988). Mineralogy, Composition, and Fluid Inclusion Microthermometry of Sea-Floor Hydrothermal Deposits in the Southern Trough of Guaymas Basin, Gulf of California. *Can. Mineral.* 26(3)567–587

Proskurowski, G., Lilley, M. D., and Olson, E. J. (2008). Stable Isotopic Evidence in Support of Active Microbial Methane Cycling in Low-Temperature Diffuse Flow Vents at 9°50'N East Pacific Rise. *Geochim. Cosmochim. Acta* 72 (8), 2005–2023. doi: 10.1016/j.gca.2008.01.025

Rees, C. E., Jenkins, W. J., and Monster, J. (1978). The Sulphur Isotopic Composition. *Geochim. Cosmochim. Acta* 42 (65), 377–381. doi: 10.1016/0016-7037(78)90268-5

Reeves, E. P., and Fiebig, J. (2020). Abiotic Synthesis of Methane and Organic Compounds in Earth's Lithosphere. *Elements: An Int. Magaz of Mineral., Geochem., and Petrol.*. 16(1), pp.25–31.doi: 10.2138/gselements.16.1.25

Reeves, E. P., Seewald, J. S., Saccocia, P., Bach, W., Craddock, P., Shanks, W. C., et al. (2011). Geochemistry of Hydrothermal Fluids From the PACMANUS, Northeast Pual and Vienna Woods Hydrothermal Fields, Manus Basin, Papua New Guinea. *Geochim. Cosmochim. Acta* 75 (4), 1088–1123. doi: 10.1016/j.gca.2010.11.008

Roedder, E. (1984). "Introduction to Fluid Inclusions." *Reviews in Mineralogy, Volume 12: Fluid Inclusions* (Mineralogical Society of America).

Rogers, A. D., Tyler, P. A., Connelly, D. P., Copley, J. T., James, R., Larter, R. D., et al. (2012). The Discovery of New Deep-Sea Hydrothermal Vent Communities in the Southern Ocean and Implications for Biogeography. *PloS Biol.* 10 (1),e1001234. doi: 10.1371/journal.pbio.1001234

Ryan, J. G., and Langmuir, C. H. (1987). The Systematics of Lithium Abundances in Young Volcanic Rocks. *Geochim. Cosmochim. Acta* 51 (6), 1727–1741. doi: 10.1016/0016-7037(87)90351-6

Sakai, H., Des Marais, D. J., Ueda, A., and Moore, J. G. (1984). Concentrations and Isotope Ratios of Carbon, Nitrogen and Sulfur in Ocean-Floor Basalts. *Geochim. Cosmochim. Acta* 48 (12), 2433–2441. doi: 10.1016/0016-7037(84)90295-3

Scheuermann, P. P., Tutolo, B. M., and Seyfried, W. E. (2019). Anhydrite Solubility in Low-Density Hydrothermal Fluids: Experimental Measurements and Thermodynamic Calculations. *Chem. Geolog.* 524 (June), 184–195. doi: 10.1016/j.chemgeo.2019.06.018

Schmidt, K., Garbe-Schönberg, D., Bau, M., and Koschinsky, A. (2010). Rare Earth Element Distribution in <400°C Hot Hydrothermal Fluids From 5°S, MAR: The Role of Anhydrite in Controlling Highly Variable Distribution Patterns. *Geochim. Cosmochim. Acta* 74 (14), 4058–4077. doi: 10.1016/j.gca.2010.04.007

Seewald, J. S., Doherty, K. W., Hammar, T. R., and Liberatore, S. P. (2002). Instruments and Methods A New Gas-Tight Isobaric Sampler for Hydrothermal Fluids. *Deep-Sea. Res. I.* 49, 189–196. doi: 10.1016/S0967-0637(01)00046-2

Seewald, J. S., Reeves, E. P., Bach, W., Saccocia, P. J., Craddock, P. R., Shanks, W. C., et al. (2015). Submarine Venting of Magmatic Volatiles in the Eastern Manus Basin, Papua New Guinea. *Geochim. Cosmochim. Acta* 163, 178–199. doi: 10.1016/j.gca.2015.04.023

Seewald, J. S., Reeves, E. P., Bach, W., Saccocia, P. J., Craddock, P. R., Walsh, W., et al. (2019). Geochemistry of Hot-Springs at the SuSu Knolls Hydrothermal Field, Eastern Manus Basin: Advanced Argillic Alteration and Vent Fluid Acidity. *Geochim. Cosmochim. Acta* 255, 25–48. doi: 10.1016/j.gca.2019.03.034

Seewald, J. S., and Seyfried, W. E. (1990). The Effect of Temperature on Metal Mobility in Subseafloor Hydrothermal Systems: Constraints From Basalt Alteration Experiments. *Earth Planet. Sci. Lett.* 101 (2–4), 388–403. doi: 10.1016/0012-821X(90)90168-W

Seewald, J. S., Seyfried, W. E., and Shanks, W. C. (1994). Variations in the Chemical and Stable Isotope Composition of Carbon and Sulfur Species During Organic-Rich Sediment Alteration: An Experimental and Theoretical Study of Hydrothermal Activity at Guaymas Basin, Gulf of California. *Geochim. Cosmochim. Acta* 58 (22), 5065–5082. doi: 10.1016/0016-7037(94)90232-1

Seyfried, W. E., and Ding, K. (1995). "Phase Equilibria in Subseafloor Hydrothermal Systems: A Review of the Role of Redox, Temperature, PH and Dissolved Cl on the Chemistry of Hot Spring Fluids at Mid-Ocean Ridges," in *Geophy. Monogr. Ser.* 248–272. doi: 10.1029/GM091p0248.

Seyfried, W. E., Ding, K., and Berndt, M. E. (1991). Phase Equilibria Constraints on the Chemistry of Hot Spring Fluids at Mid-Ocean Ridges. *Geochim. Cosmochim. Acta* 55 (12), 3559–3580. doi: 10.1016/0016-7037(91)90056-B

Seyfried, W. E., Janecky, D. R., and Mottl, M. J. (1984). Alteration of the Oceanic Crust: Implications for Geochemical Cycles of Lithium and Boron. *Geochim. Cosmochim. Acta* 48 (3), 557–569. doi: 10.1016/0016-7037(84)90284-9

Seyfried, W. E., Seewald, J. S., Berndt, M. E., Ding, K., and Foustoukos, D. I. (2003). Chemistry of Hydrothermal Vent Fluids From the Main Endeavour Field, Northern Juan De Fuca Ridge: Geochemical Controls in the Aftermath of June 1999 Seismic Events. *J. Geophys. Res.: Solid. Earth* 108 (B9), 1–23. doi: 10.1029/2002jb001957

Shanks, W. C. (2001). Stable Isotopes in Seafloor Hydrothermal Systems. *Rev. Mineral. Geochem.* 43, 469–526. doi: 10.2138/gsrmg.43.1.469

Shanks, W. C., Böhlke, J. K., and Seal, R. R. (1995). Stable Isotopes in Mid-Ocean Ridge Hydrothermal Systems: Interactions between Fluids, Minerals, and Organisms. *Geophys. Monogr. Ser.* 91), 194–221. doi: 10.1029/GM091p0194

Shmulovich, K. I., Landwehr, D., Simon, K., and Heinrich, W. (1999). Stable Isotope Fractionation between Liquid and Vapour in Water-Salt Systems up to 600°C. *Chem. Geolog.* 157 (3–4), 343–354. doi: 10.1016/S0009-2541(98)00202-2

Takai, K., Nunoura, T., Ishibashi, J. I., Lupton, J., Suzuki, R., Hamasaki, H., et al. (2008). Variability in the Microbial Communities and Hydrothermal Fluid Chemistry at the Newly Discovered Mariner Hydrothermal Field, Southern Lau Basin. *J. Geophys. Res.: Biogeosci.* 113 (G2). doi: 10.1029/2007JG000636

Taylor, B. (1979). Bismarck Sea: Evolution of a Back-Arc Basin. *Geology* 7 (4), 171–174. doi: 10.1130/0091-7613(1979)7<171:BSEOAB>2.0.CO;2

Taylor, B. E. (1986). "Magmatic Volatiles: Isotopic Variation of C, H, and S.", in *Stable Isotopes in High Temperature Geological Processes.* 16 (1), 185–225

Taylor, H. (1997). "Oxygen and Hydrogen Isotope Relationships in Hydrothermal Mineral Deposits.", in *Geochemistry of Hydrothermal Ore Deposits.* 229–302

Toki, T., Itoh, M., Iwata, D., Ohshima, S., Shinjo, R., Ishibashi, J. I., et al. (2016). Geochemical Characteristics of Hydrothermal Fluids at Hatoma Knoll in the Southern Okinawa Trough. *Geochem. J.* 50 (6), 493–525. doi: 10.2343/geochemj.2.0449

Tyler, P. A. (2012). RRS James Cook cruise JC80, 2nd Dec-30 Dec 2012. The East Scotia Ridge and Kemp Seamount Caldera, Cruise 4 of the NERC Consortium Grant 'Chemosynthetically driven ecosystems in the Southern Ocean. *Ecology and Biogeography' (ChEsSo)* (Southampton, UK: National Oceanography Centre Southampton).

Vanko, D. A., and Bach, W. (2005). Heating and Freezing Experiments on Aqueous Fluid Inclusions in Anhydrite: Recognition and Effects of Stretching and the Low-Temperature Formation of Gypsum. *Chem. Geolog.* 223 (1–3), 35–45. doi: 10.1016/j.chemgeo.2004.11.021

Vityk, M. O., Bodnar, R. J., and Schmidt, C. S. (1994). Fluid Inclusions as Tectonothermobarometers: Relation between Pressure-Temperature History and Reequilibration Morphology during Crustal Thickening. *Geology* 22 (8), 731–734. doi: 10.1130/0091-7613(1994)022<0731:FIATRB>2.3.CO;2

Von Damm, K. L., Bischoff, J. L., and Rosenbauer, R. J. (1991). Quartz Solubility in Hydrothermal Seawater: An Experimental Study and Equation Describing Quartz Solubility for up to 0.5 M NaCl Solutions. *Am. J. Sci* 291(10), pp.977–1007.. doi: 10.2475/ajs.291.10.977

Von Damm, K. L. (1990). Seafloor Hydrothermal Activity: Black Smoker Chemistry and Chimneys. *Annu. Rev. Earth Planet. Sci.* 18, 173–204. doi: 10.1146/annurev.ea.18.050190.001133

Von Damm, K. L. (1995) Controls on the Chemistry and Temporal Variability of Seafloor Hydrothermal Fluids. *Seafloor Hydrothermal Systems: Physical, Chemical, Biological, and Geological Interactions* 91, 222–247.

Von Damm, K. L., Edmond, J. M., Grant, B., Measures, C. I., Walden, B., and Weiss, R. F. (1985a). Chemistry of Submarine Hydrothermal Solutions at 21 °N, East Pacific Rise. *Geochim. Cosmochim. Acta* 49 (11), 2197–2220. doi: 10.1016/0016-7037(85)90222-4

Von Damm, K. L., Edmond, J. M., Measures, C. I., and Grant, B. (1985b). Chemistry of Submarine Hydrothermal Solutions at Guaymas Basin, Gulf of California. *Geochim. Cosmochim. Acta* 49 (11), 2221–2237. doi: 10.1016/0016-7037(85)90223-6

Von Damm, K. L., Lilley, M. D., Shanks Iii, W. C., Brockington, M., Bray, A. M., O'Grady, K. M., et al. (2003). Extraordinary Phase Separation and Segregation in Vent Fluids from the Southern East Pacific Rise. *Earth Planet. Sci. Lett.* 206 (3–4), 365–378. doi: 10.1016/S0012-821X(02)01081-6

Von Damm, K. L., Parker, C. M., Zierenberg, R. A., Lilley, M. D., Olson, E. J., Clague, D. A., et al. (2005). The Escanaba Trough, Gorda Ridge Hydrothermal System: Temporal Stability and Subseafloor Complexity. *Geochim. Cosmochim. Acta* 69 (21), 4971–4984. doi: 10.1016/j.gca.2005.04.018

Wang, D. T., Reeves, E. P., McDermott, J. M., Seewald, J. S., and Ono, S. (2018). Clumped Isotopologue Constraints on the Origin of Methane at Seafloor Hot Springs. *Geochim. Cosmochim. Acta* 223, 141–158. doi: 10.1016/j.gca.2017.11.030

Welhan, J. A. (1988). Origins of Methane in Hydrothermal Systems. *Chem. Geolog.* 71 (1–3), 183–198. doi: 10.1016/0009-2541(88)90114-3

Welhan, J. A., and Craig, H. (1983). "Methane, Hydrogen and Helium in Hydrothermal Fluids at 21°N on the East Pacific Rise.", in *Hydrothermal Processes at Seafloor Spreading Centers.* Boston, MA: Springer). 391–409. doi: 10.1007/978-1-4899-0402-7_17.

Xu, G. (2000). Fluid Inclusions with NaCl-CaCl$_2$-H$_2$O Composition from the Cloncurry Hydrothermal System, NW Queensland, Australia. *Lithos* 53 (1), 21–35. doi: 10.1016/S0024-4937(00)00008-6

Yang, K., and Scott, S. D. (2006). Magmatic Fluids as a Source of Metals in Arc/Back-Arc Hydrothermal Systems: Evidence from Melt Inclusions and Vesicles. *Back. Arc. Spread. Syst.: Geolog. Biologic. Chem. Phys. Interact. Geophys.* 1), 163–184.